SUPPORTING INFORMATION

Anticancer Agent with Inexplicable Potency in Extreme Hypoxia: Characterizing a Light-Triggered Ruthenium Ubertoxin

Houston D. Cole,[a,‡] John A. Roque III,[a,b,‡] Ge Shi,[a,‡] Liubov M. Lifshits,[a,‡] Elamparuthi Ramasamy,[a] Patrick C. Barrett,[b] Rachel O. Hodges,[b] Colin G. Cameron,[a*] Sherri A. McFarland[a*]

a Department of Chemistry and Biochemistry, The University of Texas at Arlington, Arlington, Texas, 76019-0065 United States
b Department of Chemistry and Biochemistry, The University of North Carolina at Greensboro, Greensboro, North Carolina 27402, USA
‡Contributed equally to this work
*Corresponding Authors: C.G.C <colin.cameron@uta.edu> ORCID 0000-0003-0978-0894; S.A.M. <sherri.mcfarland@uta.edu> ORCID 0000-0002-8028-5055

Contents

List of Figures and Charts

1. SYNTHETIC DETAILS

Microwave reactions were performed in a CEM Discover microwave reactor. Flash chromatography relied on the Teledyne Isco CombiFlash EZ Prep system with Silicycle SiliaSep silica flash cartridges (FLH-R10030B-ISO25). Size-exclusion chromatography was performed on a manual column packed with Sephadex® LH-20. NMR spectra were collected using Agilent 700 MHz NMR at the Joint School of Nanoscience and Nanoengineering (JSNN) at Greensboro. The chemical shifts are reported in parts per million (ppm) and were referenced to the residual solvent peaks. ESI mass spectra were obtained using a Thermo Fisher LTQ Orbitrap XL coupled to a Water's Acquity Ultra Performance Liquid Chromatography (UPLC) stack using a BEH C18 column at UNCG's Triad Mass Spectrometry facility. HPLC analyses were carried out on an Agilent/Hewlett Packard 1100 series instrument (ChemStation Rev. A. 10.02 software) using a Hypersil GOLD C18 column (Thermo 25005-254630, guard 25003-014001) with an A–B gradient (40 min run, 1 mL min^{-1}, ~25°C; 98% → 5% A; A=0.1% formic acid in H_2O, B=0.1% formic acid in MeCN). Reported retention times are accurate to within ± 0.1 min.

Ligand IP-4T (2-([2,2′:5′,2″:5″,2‴-quaterthiophen]-5-yl)-1*H*-imidazo[4,5-*f*][1,10]phenanthroline) was prepared as we previously described.[1] To the authors knowledge, compounds **1** and **2** are new and previously unpublished. Compounds **1** and **2** were characterized via NMR, ESI^+–MS, and HPLC (see below for the synthetic procedures and characterization data). The Cl^- salt of final complexes were obtained via anion metathesis on HCl-treated Amberlite IRA-410 resin (Alfa-Aesar, A1773436) using methanol as eluent followed by isolation in vacuo. Final complexes were isolated as a mixture of Δ/Λ isomers.

[Ru(6,6′-dmb)₂(IP-4T)](Cl)₂ (**1**). $Ru(6,6'\text{-dmb})_2(Cl)_2 \cdot 2H_2O$ (81 mg, 0.16 mmol) and IP-4T (88 mg, 0.16 mmol) were combined and added to a microwave vessel containing argon-purged ethylene glycol (2.5 mL) and subjected to microwave irradiation at 180 °C for 15 minutes. The resulting dark red mixture was transferred to a separatory funnel with deionized water (20 mL) and CH_2Cl_2 (30 mL). After gentle mixing, the CH_2Cl_2 was drained and the remaining aqueous layer was washed with CH_2Cl_2 (30 mL portions) until the CH_2Cl_2 was colorless. At that point, another 30 mL of CH_2Cl_2 was added and allowed to settle to the bottom of the separatory funnel. Then, saturated aqueous KPF_6 (5 mL) was added, and the mixture was shaken gently and allowed to settle over time to facilitate transfer of the product from the aqueous layer to the CH_2Cl_2 layer, which was concentrated under reduced pressure. The crude product was purified by silica gel flash column chromatography with a gradient of MeCN, 10% water in MeCN, followed by 7.5% water in MeCN with 0.5% KNO_3 to obtain the desired product as a red solid (20 mg, 10%). The PF_6^- salt was converted in quantitative yield to its corresponding Cl^- salt using Amberlite IRA-410 with MeOH as the eluent. The Cl^- salt was purified further using Sephadex LH-20 with MeOH as the eluent (16 mg, 94%). R_f = 0.22 (0.5% KNO_3, 7.5% H_2O, 92% MeCN). ^1H NMR (500 MHz, MeOD-*d₃*, ppm): δ 9.01 (d, *J* = 8.0 Hz, 2H; c), 8.76 (d, *J* = 8.0 Hz, 2H; 3), 8.55 (d, *J* = 8.0 Hz, 2H; 3′), 8.31 (d, *J* = 5.0 Hz, 2H; a), 8.28 (t, *J* = 8.0 Hz, 2H; 4), 7.91 (d, *J* = 4.0 Hz, 1H; d), 7.84 (dd, *J* = 8.0, 5.0 Hz, 2H; b), 7.74 (t, *J* = 8.0 Hz, 2H; 4′), 7.66 (d, *J* = 7.5 Hz, 2H; 5), 7.40 (d, *J* = 3.5 Hz, 1H; e), 7.35 (d, *J* = 4.0, 1H; f), 7.31 (dd, *J* = 5.0, 1.0 Hz, 1H; l), 7.24 (dd, *J* = 3.5, 1.0 Hz, 1H; j), 7.23 (d, *J* = 4.0 Hz, 1H; g), 7.21 (d, *J* = 3.5 Hz, 1H; h), 7.14 (d, *J* = 4.0, 1H; i), 7.02 (dd, *J* = 5.0, 3.5, 1H; k), 7.00 (d, *J* = 7.5 Hz, 2H; 5′), 1.97 (s, 6H; 6-Me), 1.63 (s, 6H; 6′-Me) (for hydrogen labels, see Figure S1). HRMS (ESI^+) m/z: Calcd for $C_{53}H_{40}N_8RuS_4$ $[M\text{-}2Cl]^{2+}$ 509.0646; Found: 509.0632. $[M\text{-}2Cl\text{-}H]^+$ Calcd for $C_{53}H_{39}N_8RuS_4$ 1017.1219; Found: 1017.1212. HPLC retention time: 24.07 min (96% purity by peak area).

[Ru(2,9-dmp)₂(IP-4T)](Cl)₂ (**2**). $Ru(2,9\text{-dmp})_2(Cl)_2 \cdot 2H_2O$ (100 mg, 0.16 mmol) and IP-4T (88 mg, 0.16 mmol) were combined and treated according to the procedure described for **1** to yield a red solid (86 mg, 50%). The PF_6^- salt was converted in quantitative yield to its corresponding Cl^- salt using Amberlite IRA-410 with MeOH as the eluent. The Cl^- salt was purified further using Sephadex LH-20 (66 mg, 92%). R_f = 0.32 (0.5% KNO_3, 7.5% H_2O, 92% MeCN). ^1H NMR (700 MHz, MeOD-*d₃*, ppm): δ 8.93 (bs, 2H; c), 8.82 (d, *J* = 8.4 Hz, 2H; 7), 8.36 (d, *J* = 9.1 Hz, 2H; 6), 8.35 (d, *J* = 8.4 Hz, 2H; 4), 8.19 (d, *J* = 9.1 Hz, 2H; 5), 7.92 (d, *J* = 8.4 Hz, 2H; 8), 7.87 (d, *J* = 3.5 Hz, 1H; d), 7.46 (m, 2H; b), 7.44 (d, *J* = 5.6 Hz, 2H; a), 7.38 (d, *J* = 4.2 Hz, 1H; e), 7.35 (d, *J* = 4.9 Hz, 1H; l), 7.34 (d, *J* = 7.7 Hz, 2H; 3), 7.33 (d, *J* = 3.5 Hz, 1H; f), 7.26 (d, *J* = 3.5 Hz, 1H; j), 7.23 (d, *J* = 4.2 Hz, 1H; g), 7.21 (d, *J* = 3.5 Hz, 1H; h), 7.16 (d, *J* = 3.5 Hz, 1H; i), 7.05 (dd, *J* = 4.9, 3.5 Hz, 1H; k), 2.06 (s, 6H; 9-Me), 1.82 (s, 6H; 2-Me) (for hydrogen labels, see Figure S2). ^{13}C NMR (175 MHz, MeOH-*d₃*, ppm): δ 169.96 (9), 168.19 (2), 152.27 (a), 150.84 (20), 150.16

(10), 149.73 (21), 147.68 (22,24), 141.64 (12), 139.46 (7), 138.49 (14), 138.26 (16), 138.20 (4), 137.84 (17), 136.39 (15), 136.16 (13), 131.96 (c,23), 131.66 (11), 131.63 (18), 131.44 (19), 129.72 (d), 129.11 (k), 128.80 (6), 128.59 (8), 128.53 (5), 127.72 (3), 126.96 (f), 126.26 (b), 126.09 (h,l), 125.87 (e), 125.81 (g), 125.57 (i), 125.12 (j), 26.97 (2-Me), 25.46 (9-Me) (for carbon labels, see Figure S3). HRMS (ESI$^+$) m/z: $[M-2Cl]^{2+}$ Calcd for $C_{57}H_{40}N_8RuS_4$ 533.0646; Found: 533.0634. $[M-2Cl-H]^+$ Calcd for $C_{57}H_{39}N_8RuS_4$ 1065.1219; Found: 1065.1220. HPLC retention time: 24.35 min (98% purity by peak area).

2. NMR SPECTRA

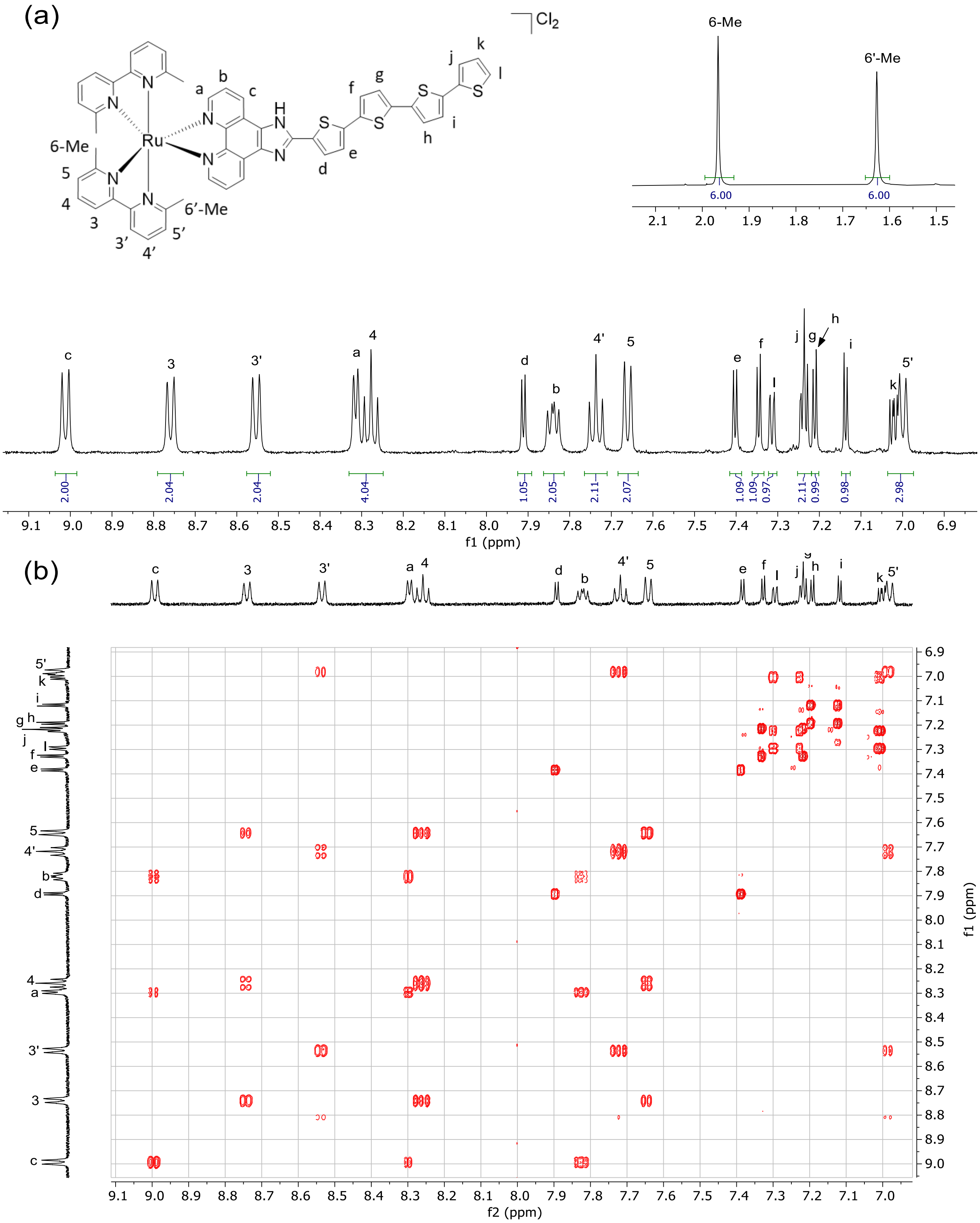

Figure S1. 500 MHz ^{1}H NMR spectra of **1** (Cl$^-$ salt) in MeOD-d_3 at 298 K with structure labelling and ^{1}H NMR assignments. (a) Zoom of ^{1}H NMR spectrum, aromatic region; the inset shows aliphatic region. (b) ^{1}H–^{1}H COSY NMR spectrum, aromatic region.

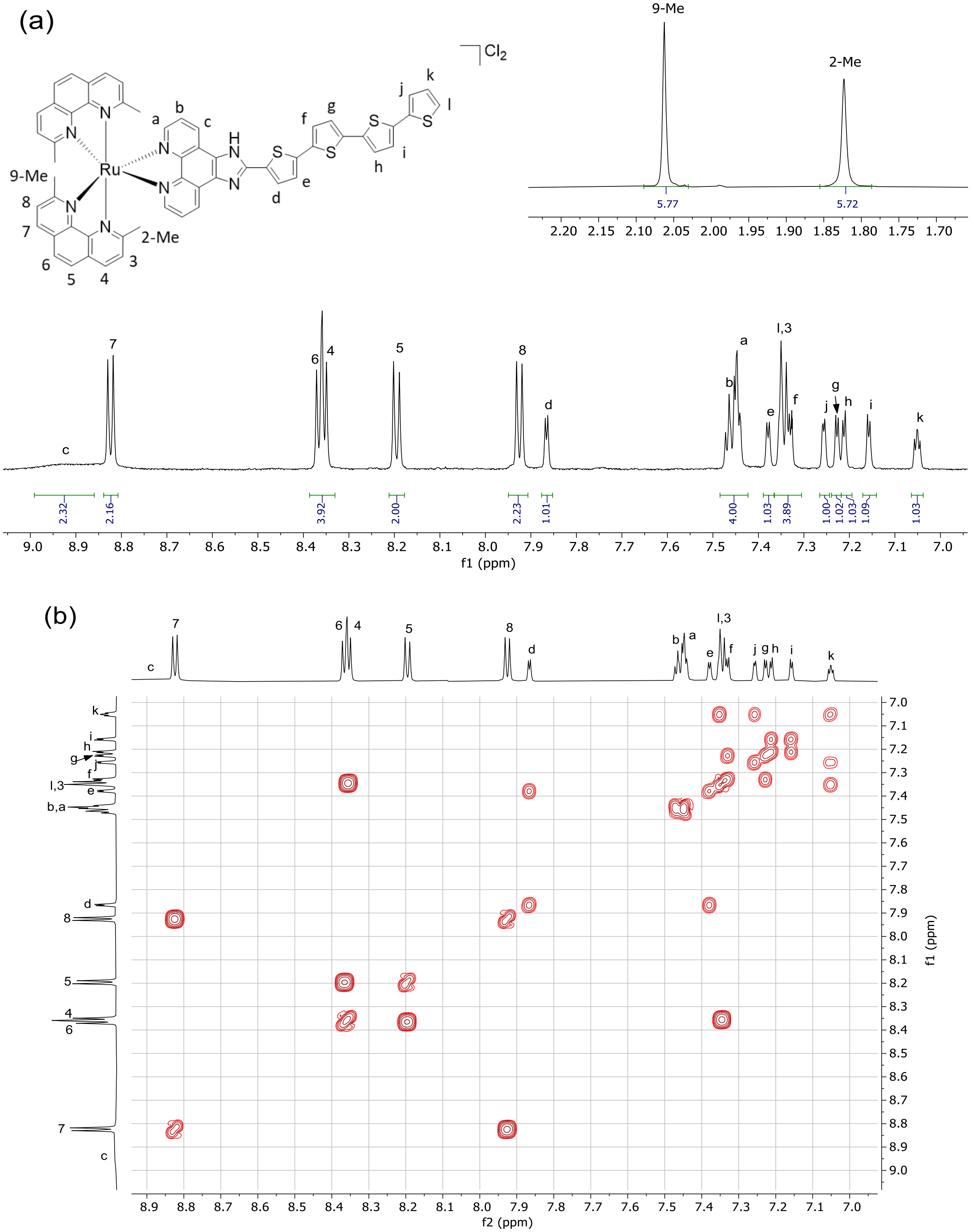

Figure S2. 700 MHz ^{1}H NMR spectra of **2** (Cl$^-$ salt) in MeOD-*d*$_3$ at 298 K with structure labelling and ^{1}H NMR assignments. (a) Zoom of ^{1}H NMR spectrum, aromatic region; the inset shows aliphatic region. (b) ^{1}H–^{1}H COSY NMR spectrum, aromatic region.

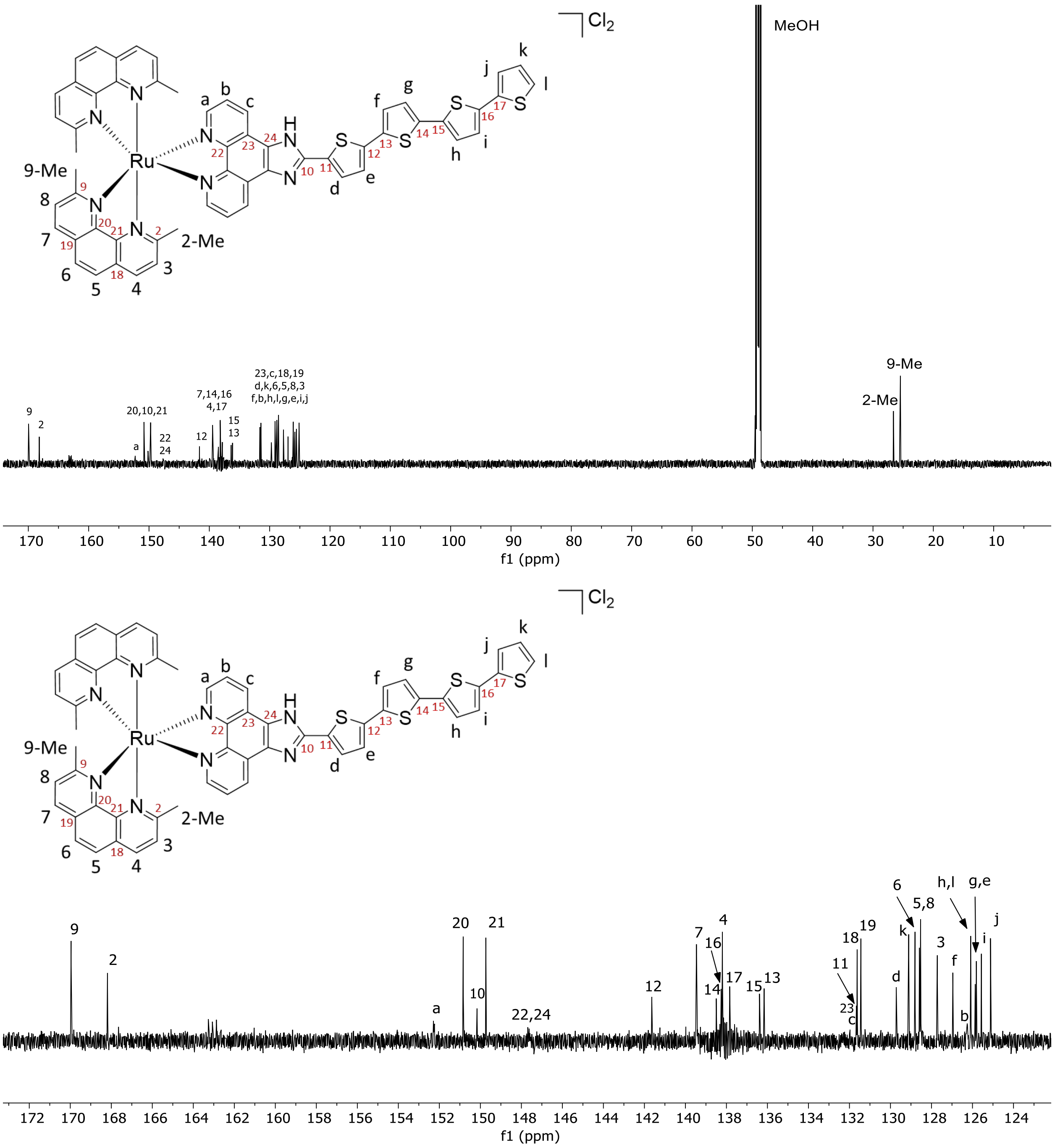

Figure S3. 175 MHz ^{13}C NMR spectrum of **2** (Cl$^-$ salt) in MeOD-*d_3* at 298 K with structure labelling and ^{13}C NMR assignments. Top: full region; bottom: zoom of aromatic region.

Note: Additional baseline noise is an artifact caused by nearby radio transmitters.

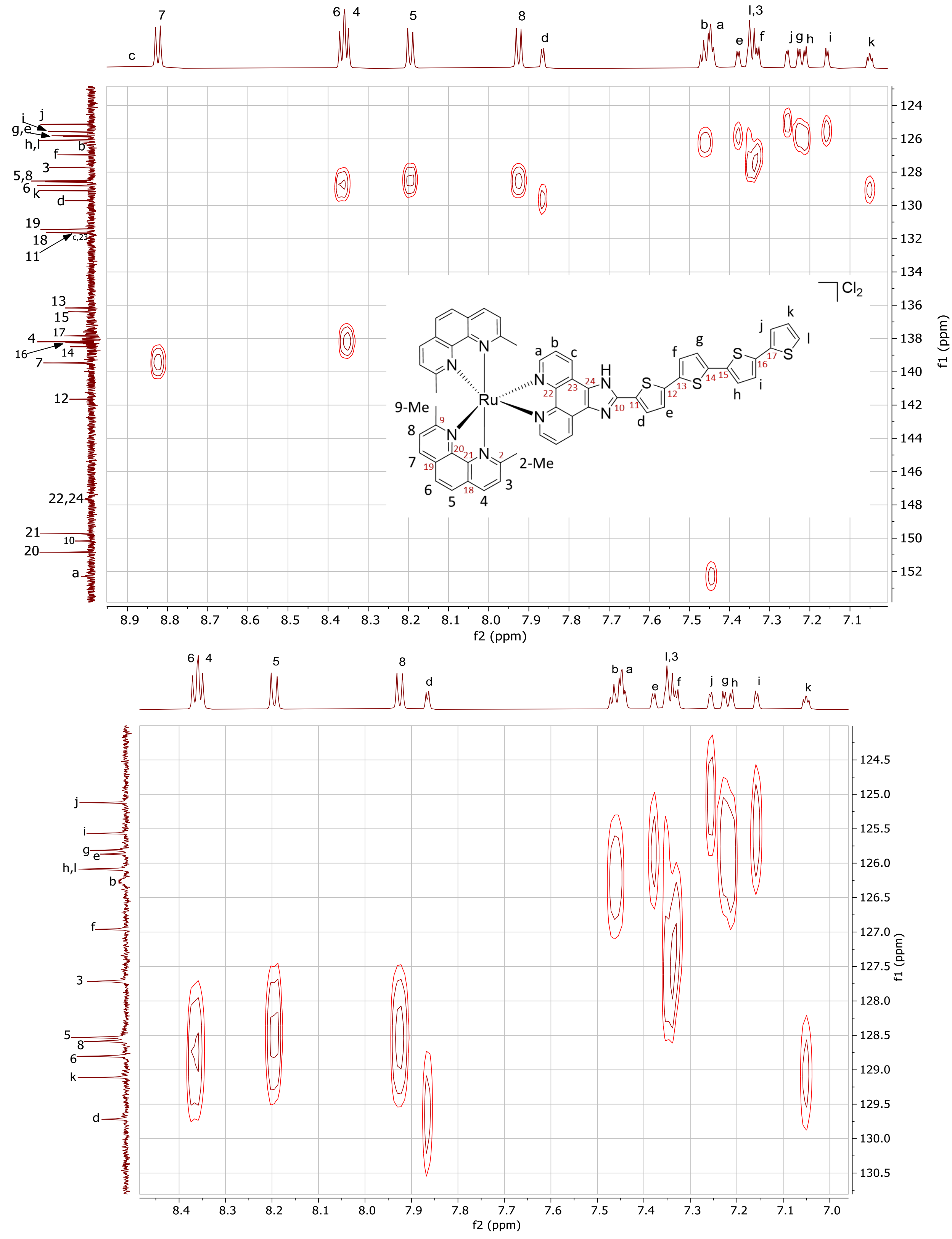

Figure S4. 700 MHz ^{13}C–^{1}H HSQC NMR spectrum of **2** (Cl^{-} salt) in MeOD-d_3 at 298 K with structure labelling and ^{1}H and ^{13}C NMR assignments, aromatic region

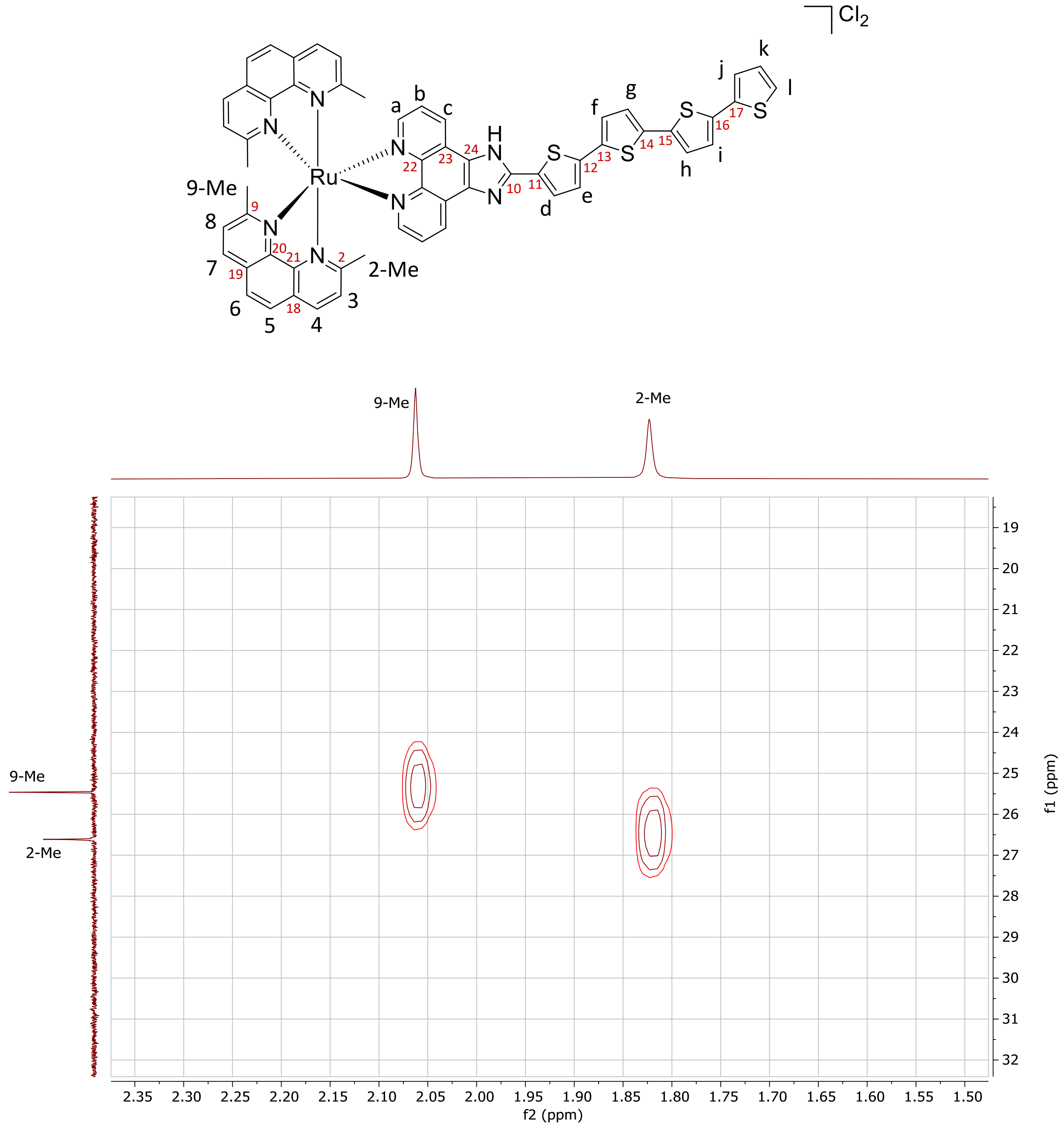

Figure S5. 700 MHz ^{13}C–^{1}H HSQC NMR spectrum of **2** (Cl^{-} salt) in MeOD-*d*$_3$ at 298 K with structure labelling and ^{1}H and ^{13}C NMR assignments, aliphatic region.

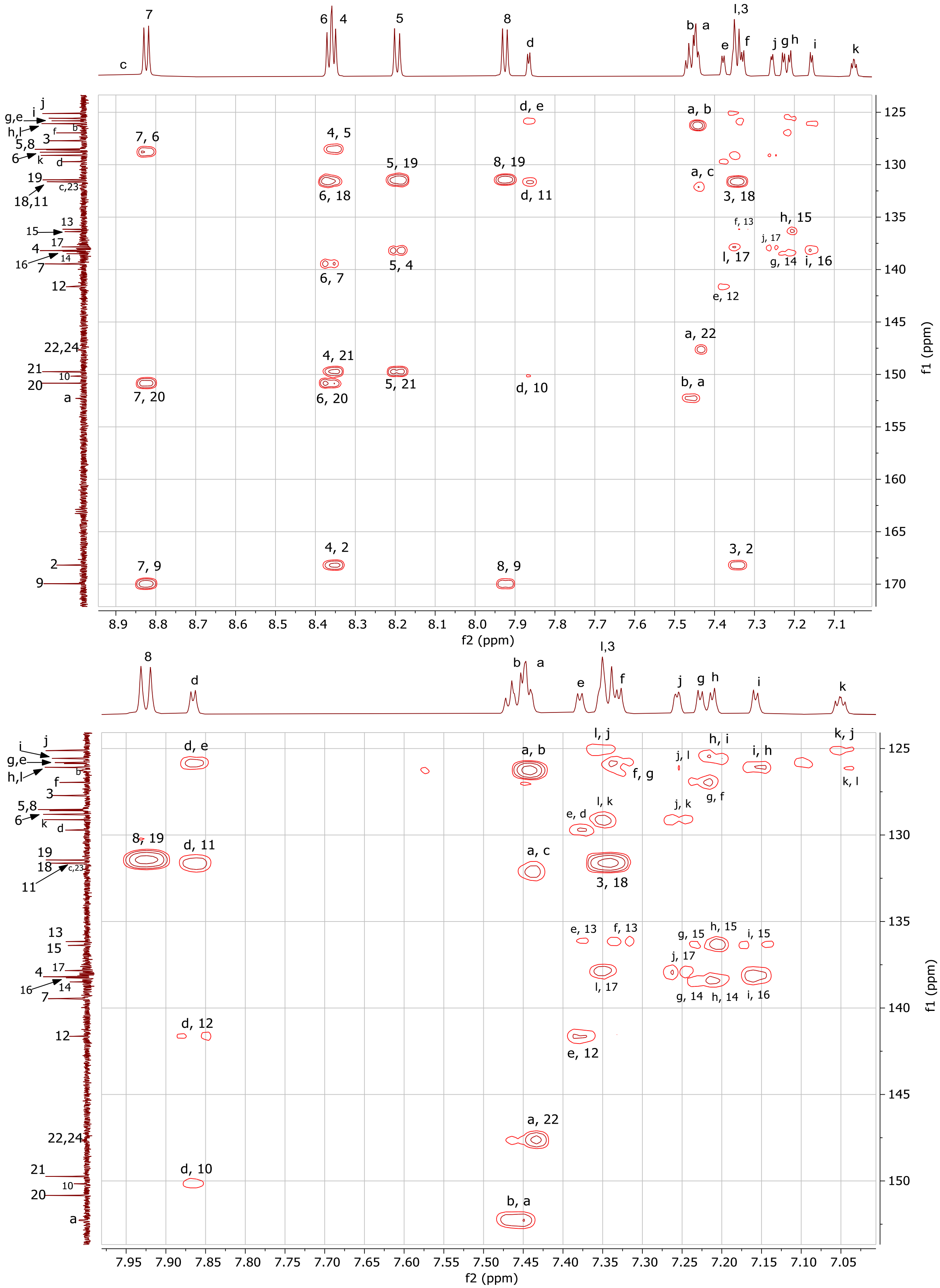

Figure S6. 700 MHz ^{13}C–^{1}H HMBC NMR spectrum of **2** (Cl^- salt) in MeOD-d_3 at 298 K with ^{1}H and ^{13}C NMR assignments, aromatic region. The signal is slightly increased in the bottom figure to show weaker correlations more prominently.

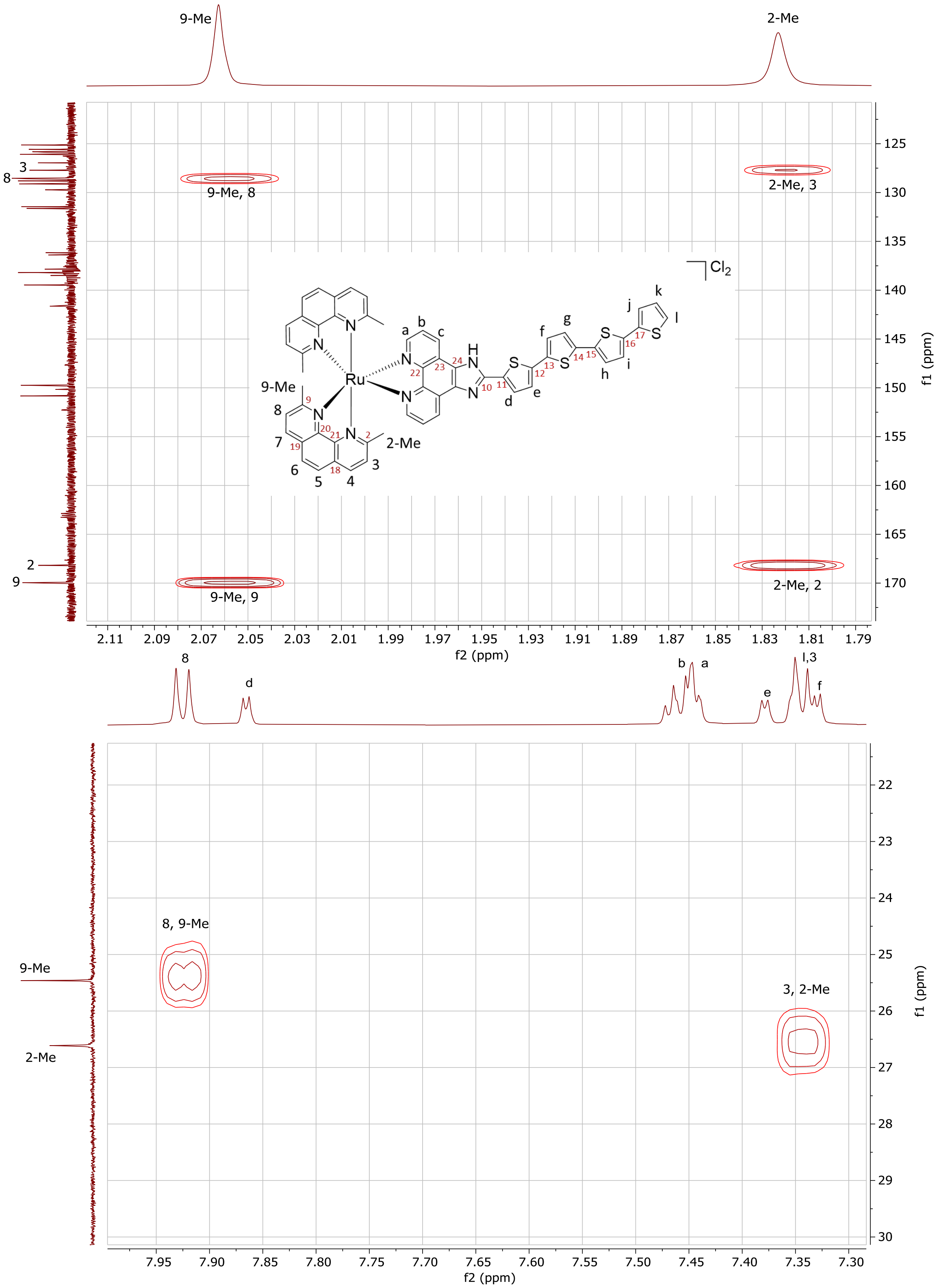

Figure S7. 700 MHz ^{13}C–^{1}H HMBC NMR spectrum of **2** (Cl^{-} salt) in MeOD-d_3 at 298 K with ^{1}H and ^{13}C NMR assignments, aliphatic ^{1}H region.

3. DESCRIPTION OF ^{1}H NMR ASSIGNMENTS

3.1 Compound 1 [Ru(6,6′-dmb)$_2$(IP-4T)](Cl)$_2$

Chart S1. Hydrogen labels used in ^{1}H NMR assignments of **1**.

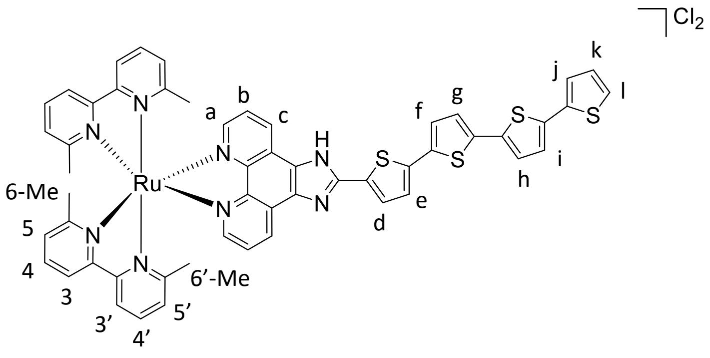

Hydrogen labels used in ^{1}H NMR assignments of **1** are shown in Chart S1.

Tris-homoleptic compound [Ru(bpy)$_3$](Cl)$_2$, which was characterized in detail by Pazderski *et al.*,[2] was used to establish the positions of signals *3–5* and *3′–5′* in complex **1**. Hydrogens from 6,6′-dimethyl-2,2′-bipyridine (6,6′-dmb) ligands followed the pattern *3* > *4* > *5* and *3′* > *4′* > *5′* (where ">" indicates further downfield). In each pair of what would be an identical position in a free non-coordinated ligand (*3* vs *3′*, *4* vs *4′*, *5 vs 5′*), the chemical shifts of hydrogens were distinctly different. This difference in chemical shifts is dictated by the strength of a shielding effect experienced by these hydrogens caused by the spatial proximity of the π-system of a neighboring ligand. Hydrogens *3*, *4*, *5* are shielded by the π-system of a neighboring 6,6′-dmb ligand, and hydrogens *3′*, *4′*, *5′* are shielded by the π-system of the neighboring IP-4T ligand. The coplanar and rigid phenanthroline core of the IP-4T ligand causes a stronger shielding effect than the more flexible 6,6′-dmb ligand. Additionally, the steric clash caused by the methyl groups forces 6,6′-dmb ligand to be positioned further away from the neighboring 6,6′-dmb ligand than from the neighboring IP-4T ligand, which also contributes to the weakening of the shielding effect on hydrogens *3*, *4*, *5*. This resulted in hydrogens *3′*, *4′*, *5′* appearing significantly more upfield than their *3*, *4*, *5* counterparts. We observed similar patterns for related Os(II) complexes.[1,3] The difference in chemical shifts between primed and non-primed positions is most pronounced for the hydrogens that are the closest in space to the IP-4T ligand (the largest difference is observed for position 5/5′). Hydrogens 3 and 3′, which are oriented away from the IP-4T, are affected the least, but their chemical shifts are still distinctly different.

Methyl groups 6-Me and 6′-Me were assigned as 6-Me > 6′-Me, following the pattern 3 > 3′; 4 > 4′; and 5 >5′.

Hydrogens from the IP-4T ligand (hydrogens *a–l*) were assigned in a similar way as described for compound **2** (below) and for related Os(II) complexes.

3.2 Compound 2 [Ru(2,9-dmp)$_2$(IP-4T)](Cl)$_2$

Chart S2. Hydrogen labels (black) and carbon labels (red) used in NMR assignments of **2**.

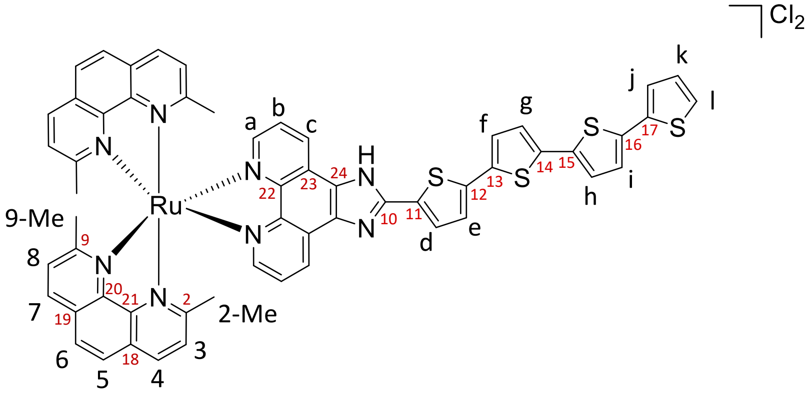

Hydrogen and carbon labels used in ^{1}H and ^{13}C peak assignments of **2** are shown in Chart S2.

Tris-homoleptic compound [Ru(phen)$_3$](Cl)$_2$, which was characterized in detail by Pazderski *et al.*,[2] was used to establish the positions of signals *3–8* in complex **2**. Hydrogens from 2,9-dimethylphenanthroline (2,9-dmp) ligands followed the pattern *4* > *5* > *3* and *7* > *6* > *8* (where ">" indicates further downfield). In each pair of what would be an identical position in a free non-coordinated ligand (*4* vs *7*, *3* vs *8*, *5 vs 6*), the chemical shifts of hydrogens were distinctly different. This difference in chemical shifts is dictated by the strength of a shielding effect experienced by these hydrogens caused by the spatial proximity of the π-system of a neighboring ligand. Hydrogens *6*, *7*, *8* are shielded by the π-system of a neighboring 2,9-dmp ligand, and hydrogens *3*, *4*, *5* are shielded by the π-system of the neighboring IP-4T ligand. Phenanthroline core of the IP-*n*T ligand causes a stronger shielding effect than the phenanthroline core of 2,9-dmp ligand, due to the steric clash caused by the methyl groups that forces 2,9-dmp ligand to be positioned further away from the neighboring 2,9-dmp ligand than from the neighboring IP-4T ligand. This resulted in hydrogens *3*, *4*, *5* appearing significantly more upfield than their *6*, *7*, *8* counterparts. We observed similar patterns for related Os(II) complexes. The difference in chemical shifts is most pronounced for the hydrogens that are the closest in space to the IP-4T ligand (the largest difference is observed for position *3*/*8*). Hydrogens *5* and *6*, which are oriented away from the IP-4T, are affected the least, but their chemical shifts are still distinctly different.

Spin system *a*-*b*-*c* was assigned next, in the following order of decreasing chemical shift: *c* > *a* = *b,* with *c* being the most downfield positioned hydrogen in the complex. Hydrogen *b* (*meta*-positioned relative to the coordinated nitrogen) typically appear the most upfield of the three in complexed phenanthroline ligands, but in this case its chemical shift coincided with the chemical shift of *b*. Hydrogen *a* (*ortho*-positioned relative to the coordinated nitrogen) was shifted upfield relative to *c* due to its proximity to the Ru(II) center, which caused a shielding effect on the nearest hydrogen.[2] Hydrogen *c* (*para*-positioned relative to the coordinated nitrogen) was too far away to be influenced by this effect. Additionally, hydrogen *c* is near the non-coordinated nitrogens of the IP-*n*T ligand, which causes a pronounced deshielding effect. It should be noted that while all other hydrogens appear on the spectrum as sharp signals, hydrogen *c* sometimes appears significantly broadened. This observed broadening is attributed to the proximity of the nitrogens of the -N=-NH- imidazo group of the IP-4T ligand and the extent of the broadening varies from sample to sample (concentration and solvent dependence).

It should also be noted that due to the quick exchange between the two nitrogens of the imidazole ring in solution, and the quick deuterium exchange with the solvent, the signal for the imidazole-NH hydrogen was not observed, similarly to literature examples.[4–6]

Among the hydrogens associated with the thiophene rings of complex **2**, hydrogens *d* and *k* were the most diagnostic. Hydrogen *d* appeared the most downfield of all thiophene hydrogens due to the strong deshielding effect of the neighboring imidazo nitrogens. Hydrogen *e* was then readily identified *via* correlation to *d* observed in ^{1}H–^{1}H COSY NMR. The most shielded hydrogen appeared as a distinct doublet of doublets and corresponded to hydrogen *k* (the middle hydrogen of the most distal thiophene ring). Hydrogens *j* and *l* were then readily identified *via* their correlations to *k* observed in ^{1}H–^{1}H COSY NMR. Hydrogen *l* was assigned as more downfield than *j*, due to *l* being deshielded by the neighboring sulfur.

Assigning the signals for the internal thiophenes (those flanked on both sides by other thiophene rings) required ^{13}C, ^{13}C–^{1}H HSQC and ^{13}C–^{1}H HMBC NMR experiments (Figure S3–Figure S7). Firstly, two internal spin systems *f*-*g* and *h*-*i* were established using ^{1}H–^{1}H COSY correlations. Next, ^{13}C–^{1}H HSQC data was used to identify which ^{13}C peaks corresponded to the thiophene hydrogens *d–l*. Then, ^{13}C–^{1}H HMBC data was used to establish diagnostic correlations, starting with hydrogens *d* and *e*. The quaternary ^{13}C signal that hydrogen *d* correlated to the strongest was assigned as carbon *11* (around 131.7 ppm), and the quaternary ^{13}C signal that hydrogen *e* correlated to the strongest was assigned as carbon *12* (around 141.6 ppm). In addition to correlations with *d* and carbon *12*, hydrogen *e* correlated with an additional quaternary carbon, which led to the assignment of this carbon as *13*. The hydrogen that carbon *13* correlated to the strongest was assigned as hydrogen *f*. Hydrogen *g* was then readily identified *via* correlation to *f* observed in ^{1}H–^{1}H COSY NMR. Next, based on the assignment of hydrogen *g*, a quaternary ^{13}C signal around 136.4 ppm was assigned as *15*. Carbon *15* exhibited correlations to both hydrogens *h* and *i*, and hydrogen *h* was assigned as the one that shows stronger correlation to carbon *15*. Lastly, hydrogen *i* was then readily identified via correlation to *h* observed in ^{1}H–^{1}H COSY NMR.

Methyl groups 2-Me and 9-Me were assigned as 9-Me > 2-Me, following the pattern 8 > 3; 7 > 4; and 6 >5. The assignment was also confirmed by the correlations observed in ^{13}C–^{1}H HMBC NMR (Figure S7).

4. HIGH RESOLUTION ESI$^+$ MASS SPECTRA

(a)

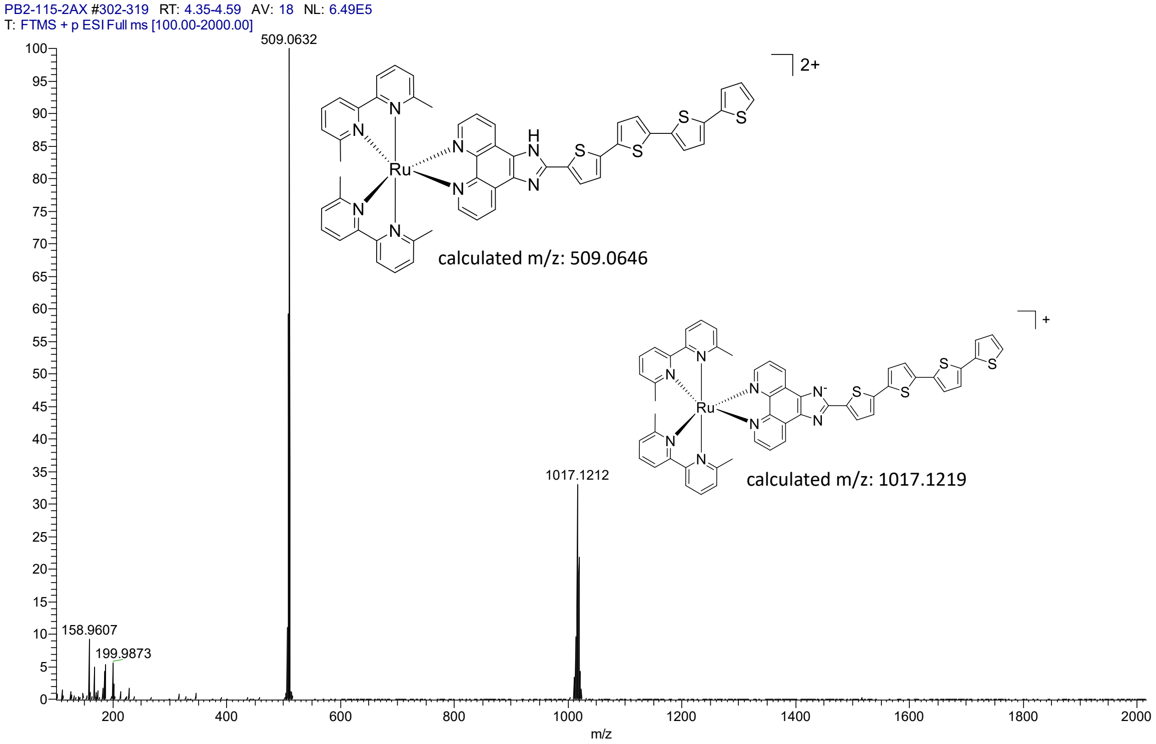

(b)

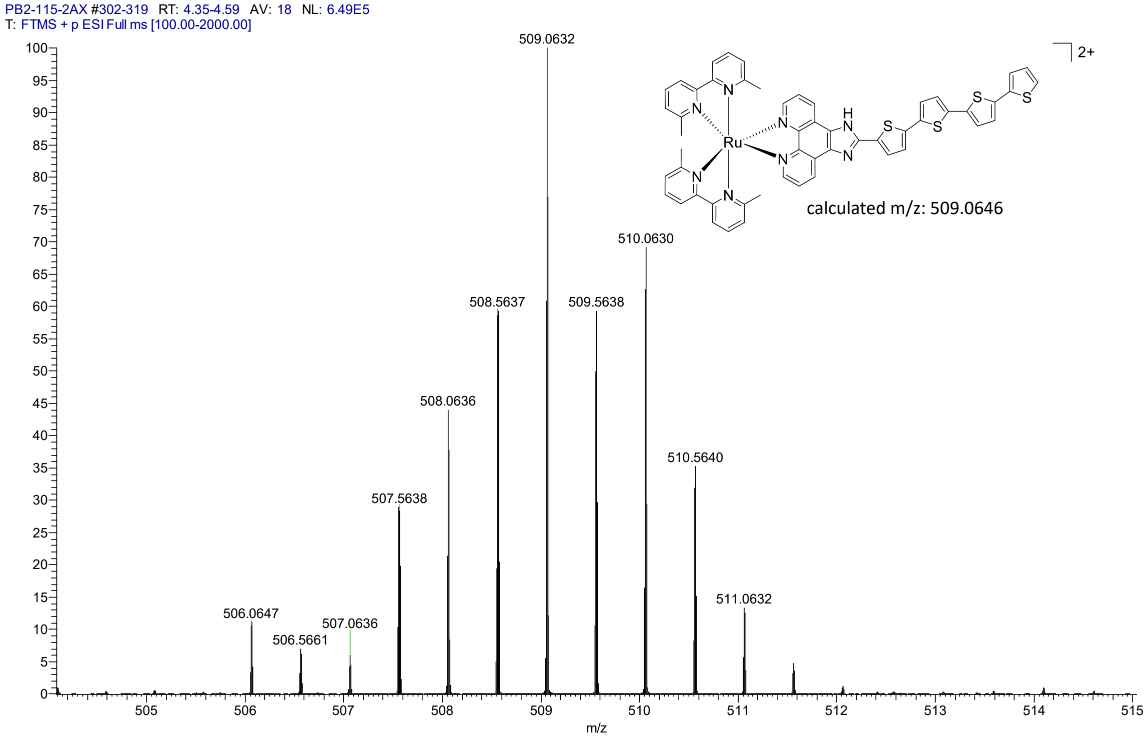

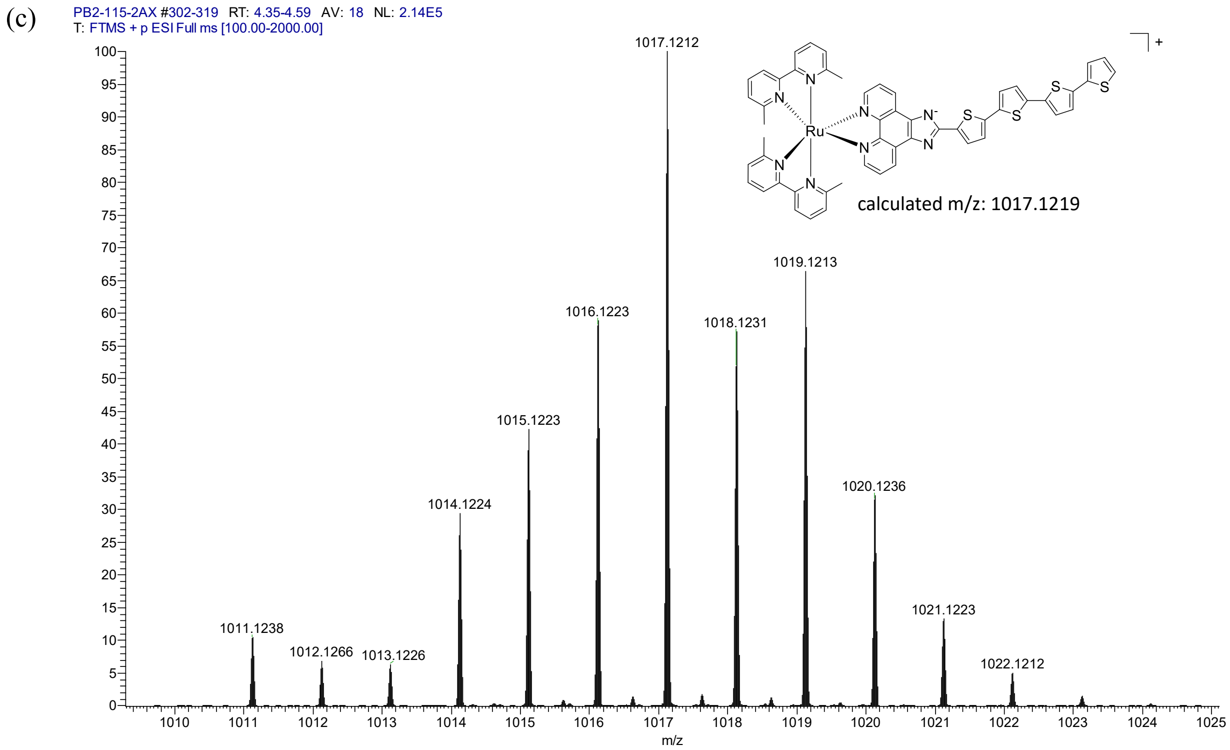

Figure S8. (a) High resolution ESI$^+$–MS spectrum for 1. (b) Zoom of 509.0632 peak showing isotopic distribution. (c) Zoom of 1017.1212 peak showing isotopic distribution.

(a)

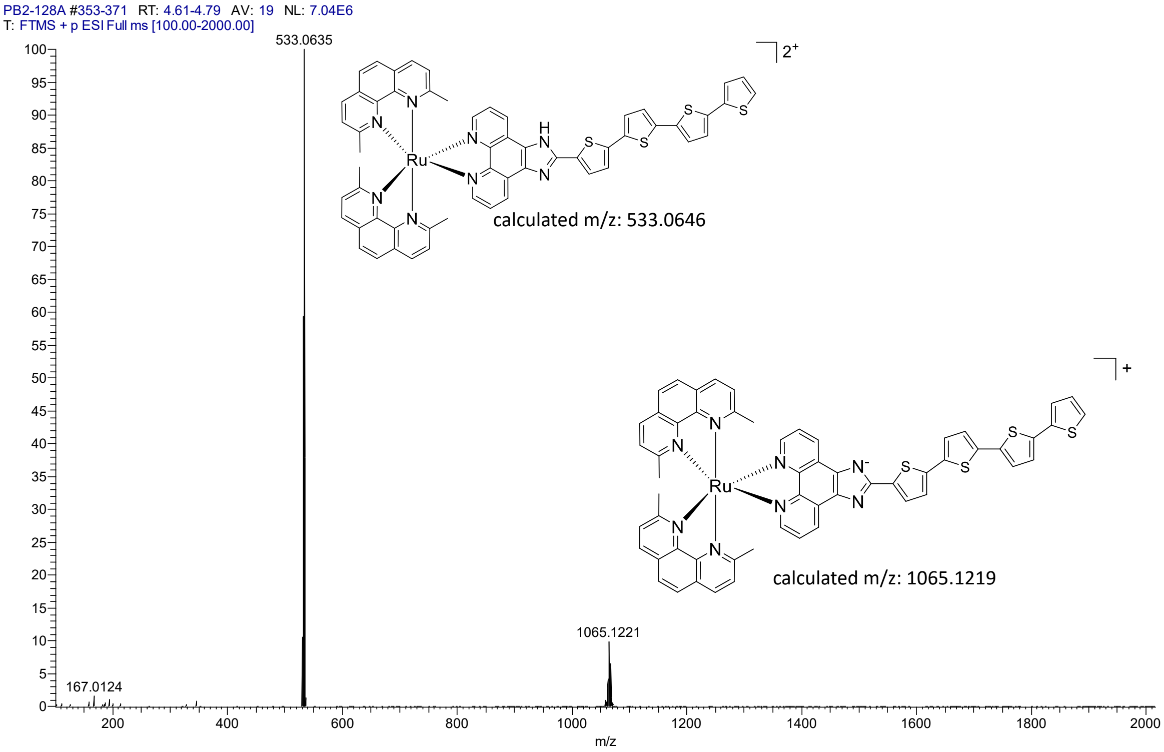
PB2-128A #353-371 RT: 4.61-4.79 AV: 19 NL: 7.04E6
T: FTMS + p ESI Full ms [100.00-2000.00]
533.0635
1065.1221
167.0124
2+
+
Ru
N
H
S
calculated m/z: 533.0646
calculated m/z: 1065.1219
0
5
10
15
20
25
30
35
40
45
50
55
60
65
70
75
80
85
90
95
100
200
400
600
800
1000
1200
1400
1600
1800
2000
m/z

(b)

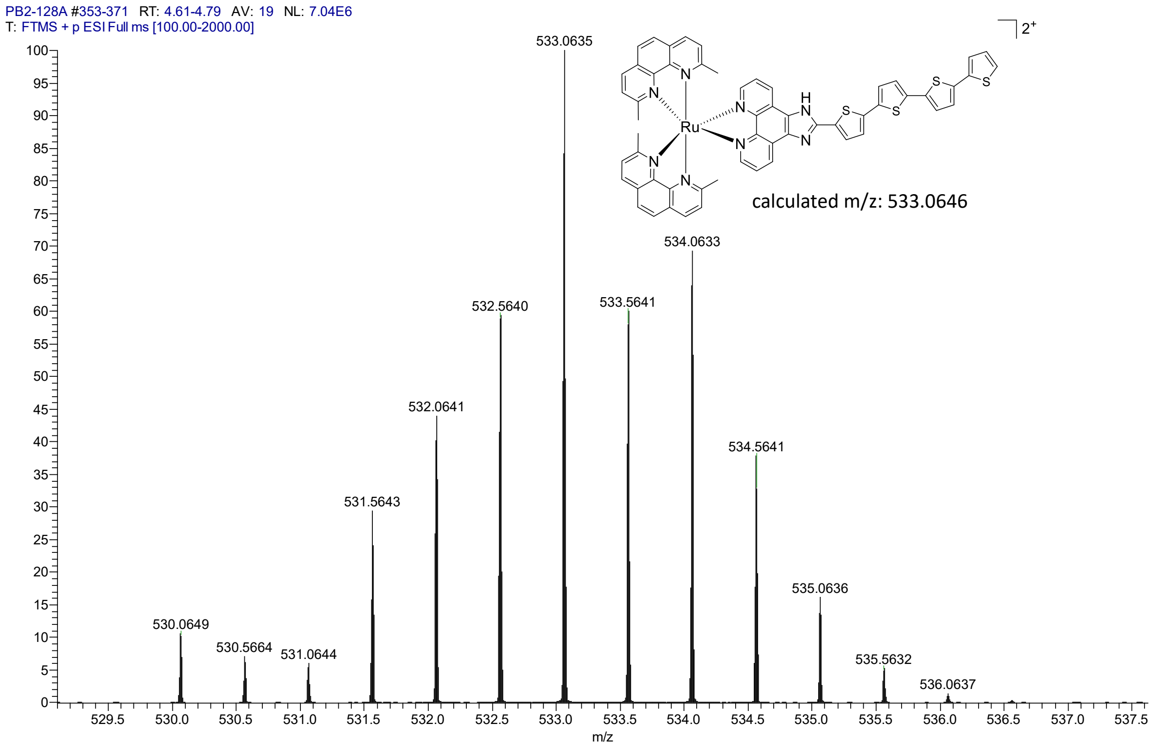
PB2-128A #353-371 RT: 4.61-4.79 AV: 19 NL: 7.04E6
T: FTMS + p ESI Full ms [100.00-2000.00]
2+
Ru
N
H
S
calculated m/z: 533.0646
533.0635
534.0633
532.5640
533.5641
532.0641
534.5641
531.5643
535.0636
530.0649
530.5664
531.0644
535.5632
536.0637
529.5
530.0
530.5
531.0
531.5
532.0
532.5
533.0
533.5
534.0
534.5
535.0
535.5
536.0
536.5
537.0
537.5
m/z

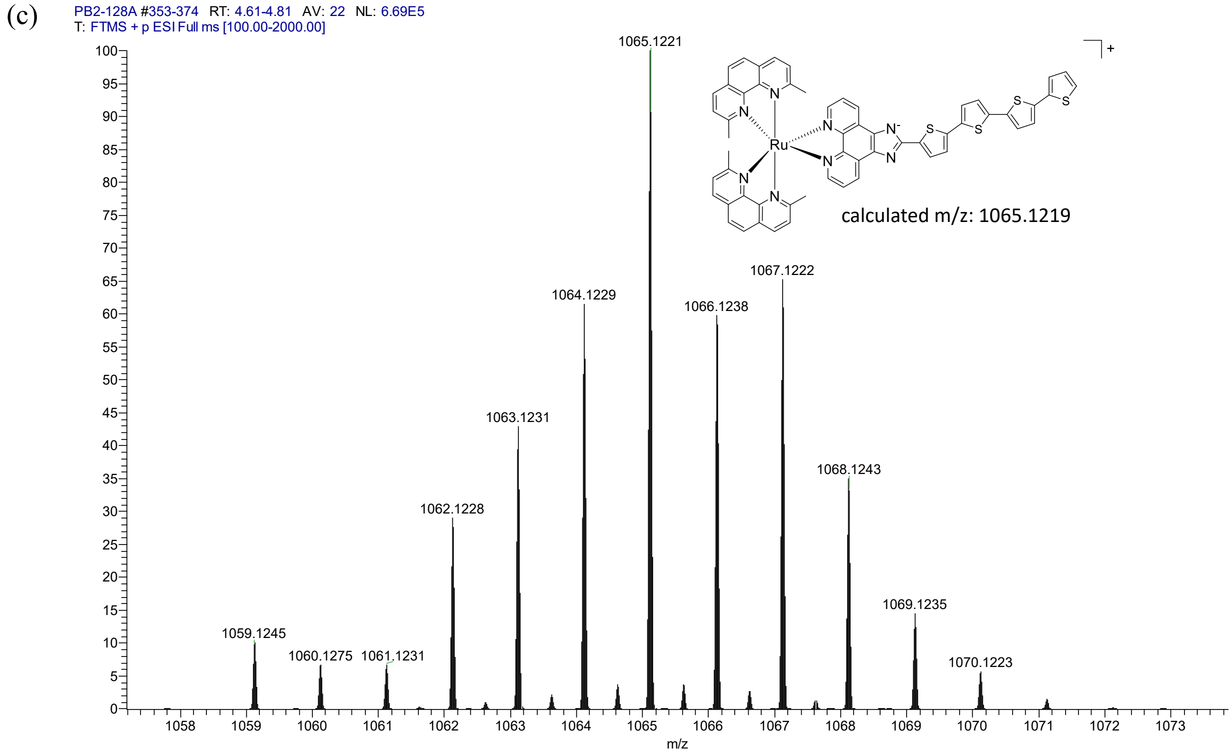

Figure S9. (a) High resolution ESI$^+$–MS spectrum for **2**. (b) Zoom of 533.0635 peak showing isotopic distribution. (c) Zoom of 1065.1221 peak showing isotopic distribution.

5. HPLC CHROMATOGRAMS

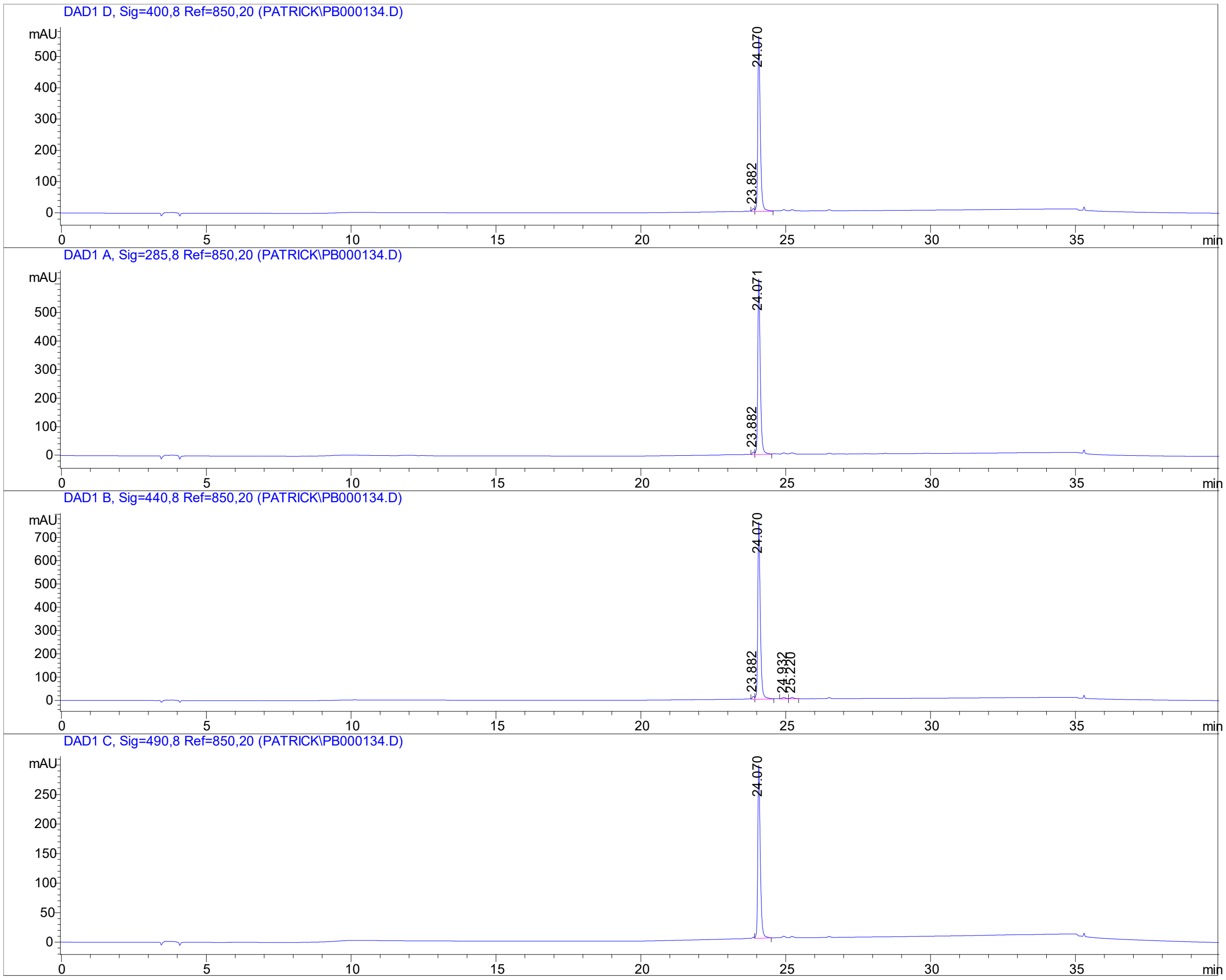

Figure S10. HPLC chromatogram for **1** collected at the following wavelengths: 400, 285, 440, and 490 nm.

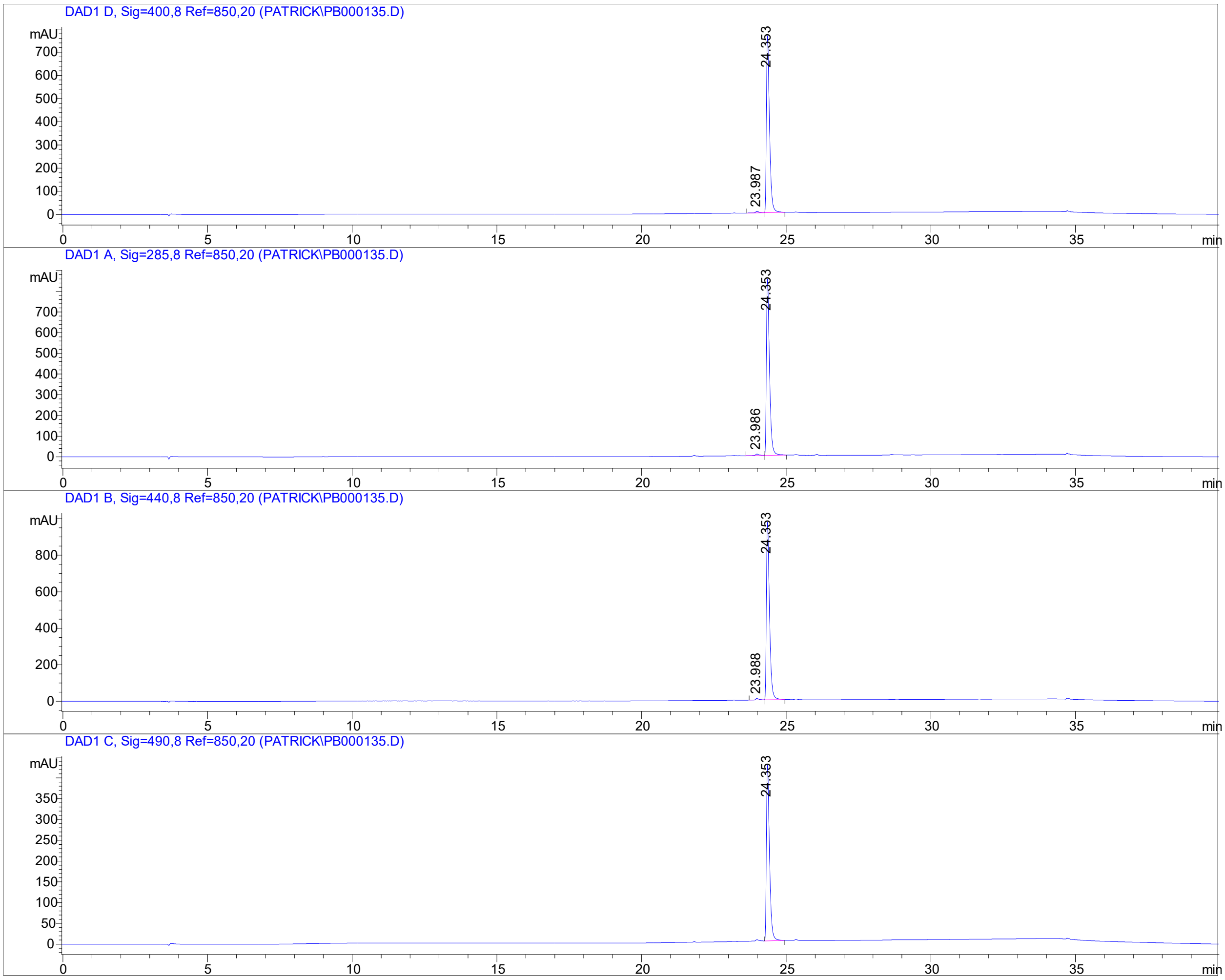

Figure S11. HPLC chromatogram for **2** collected at the following wavelengths: 400, 285, 440, and 490 nm.

6. PHOTOCHEMISTRY METHODS

6.1 Singlet Oxygen

The quantum yield for singlet oxygen sensitization (Φ_Δ) was calculated from the $^1O_2$ emission area integration centered at 1276 nm. $[Ru(bpy)_3]^{2+}$ was the standard (Φ_Δ = 0.56 in aerated MeCN[7]) using the actinometry approach in Equation S1, where *I* is the integrated emission peak, *A* is the UV-vis absorption of the solution at λ_{ex}. The solvent's refractive index η can be disregarded since $\eta^2/\eta_S{}^2=1$ due to using MeCN in all samples. The standard is denoted in the equation by the subscript *S*.

$$\Phi_\Delta = \Phi_{\Delta,S}\left(\frac{I}{I_S}\right)\left(\frac{A_S}{A}\right)\left(\frac{\eta^2}{\eta_S^2}\right) \qquad \text{Equation S1}$$

Singlet oxygen sensitization was measured in solutions of the PF_6^- salts in MeCN because water does not necessarily emulate physiological conditions (i.e., cellular membrane or proteins) and quenches the $^1O_2$ state,[8–10] leading to very short lifetimes. Additionally the MeCN/PF_6^- system is common in the literature,[11] thus facilitating comparison. The $^1O_2$ emission was measured over 1200–1350 nm using a 1000 nm long-pass filter, was baseline corrected, and excited with the longest wavelength excitation maxima, occurring at 400–465 nm. Compounds **1** and **2** were measured at 5 µM. Values were generally reproducible within ± 5%.

6.2 Photosubstitution

Chloride salts of compounds **1** and **2** were prepared at 1 mM in water (type 1, ≥ 18.2 MΩ·cm) as stock solutions and stored foiled at −20°C when not in use. Solutions were diluted to 10 µM in water and treated with visible light as reported previously at progressively increasing fluences for (a) 6 intervals of 5 s until 30 s, (b) two intervals of 15s until 1 min total, (c) 10 intervals of 30 s until 5 min total, (d) 5 intervals of 1 min until 10 min total, (e) eight 5 min intervals until 50 min, (f) five 10 min intervals, and (g) 30 min intervals until completion.[12] Samples were analysed once in 5 mm pathlength quartz cuvettes. Due to significant agglomeration-related change of the ILCT band used for monitoring **2** (and poor kinetic fit), the 10 µM solution was allowed to equilibrate for 3 h prior to initiating the experiment. Using Equation S2, kinetic analysis included the normalized change over time with respect to initial absorbance values.

$$\Delta A_n = \frac{(A_{1,n} - A_{2,n}) - (A_{1,i} - A_{2,i})}{(A_{1,f} - A_{2,f}) - (A_{1,i} - A_{2,i})} \qquad \text{Equation S2}$$

Where Equation S2 describes the absorbance change over time due to light treatment (time = *n*) where A is absorbance, subscripts 1 and 2 denote two representative wavelengths changing positively or negatively around the isosbestic point, and subscripts *i*, *n*, and *f* are the initial, nth, and final time points, respectively. The two representative wavelengths were selected based on their maximum signal change around the isosbestic wavelength. Using Graphpad Prism 8.4.1 software, mono or biexponential fits were applied as either one- or two-phase associations with the least squares method, respectively. For poor fits with monoexponential models, the extra-sum-of-squares F-test ($p<0.05$) was used to compare to a biexponential model.

The absorbance vs. time data was collected over the entire time course of the reaction. However, kinetic parameters derived from fits of these data were not included in the manuscript because photochemical byproducts build up during the course of the reaction. These photoproducts also absorb photons and have different extinction coefficients than the starting materials at the wavelength(s) being analyzed. Therefore, it is not correct to fit the data over the entire time course of the reaction. We did, however, apply fits over the first 5 s to determine qualitatively that compound **1** underwent a much faster photoreaction than **2**.

Photosubstitution quantum yields (Φ_{PS}) were calculated (Equation S3 through Equation S5) based on the spectral change after 5 s illumination, assumed a flat surface for photon flux, and corrected for overlap of the visible light source and PS absorption. No corrections were made for reflection or back-scatter. A threshold of 0.27% was applied for the light source output and shown in an overlay with the PSs (Figure S24).

$$N_p = \frac{I}{h\nu} \qquad \text{Equation S3}$$

$$E_{QF} = \frac{N_p}{N_A} \qquad \text{Equation S4}$$

$$\phi_{PS} = \frac{\Delta A_n \times \#mol_{cmpd}}{t_n \times S.A. \times \sum_{250nm}^{700nm}(1-T) \times Em_{L.S.} \times E_{QF}} \qquad \text{Equation S5}$$

Where N_P is the photon flux (photons m^{-2} s^{-1}), I is the irradiance (W m^{-2}), h=6.626×10^{-34} J s, v is the wavelength frequency (s^{-1}), E_{QF} is the molar photon flux ($mol_{photons}$ m^{-2} s^{-1}), N_A=6.022×10^{23} photons mol^{-1}, Φ_{PS} is the photosubstitution quantum yield, ΔA_n is the normalized absorbance change at time n (Equation S2), $\#mol_{cmpd}$ is the number of mol of compound at t=0, t_n is the time of illumination at n (s), *S.A.* is the sample surface area (m^2), T is transmittance at t=0 to facilitate approximation, and $Em_{L.S.}$ is the fraction of the total light source emission for a given wavelength.

Photoselective ligand loss of 6,6′-dmb and 2,9-dmp verified by ^{1}H NMR, HPLC, and ESI$^+$-MS.

Compounds **1** and **2** were prepared at 1 mM in MeOD-d_3 in NMR tubes. The samples were analyzed by HPLC, ESI$^+$-MS, and ^{1}H NMR before and after irradiation. HPLC and MS samples were prepared by removing aliquots from the 1 mM solutions and diluting with optima-grade MeOH to achieve concentrations appropriate for HPLC (300 μM) and high resolution ESI$^+$-MS (1 μM). The samples were irradiated at 20 mW cm^{-2} using a LEPOWER ZSTGD-50W Flood light for 2 hours and then analyzed by HPLC, ESI$^+$-MS, and ^{1}H NMR. To verify the identity of the liberated ligand by ^{1}H NMR, the irradiated samples were spiked with 1.25 mM 6,6'-dmb (**1**) or 2,9-dmp (**2**).

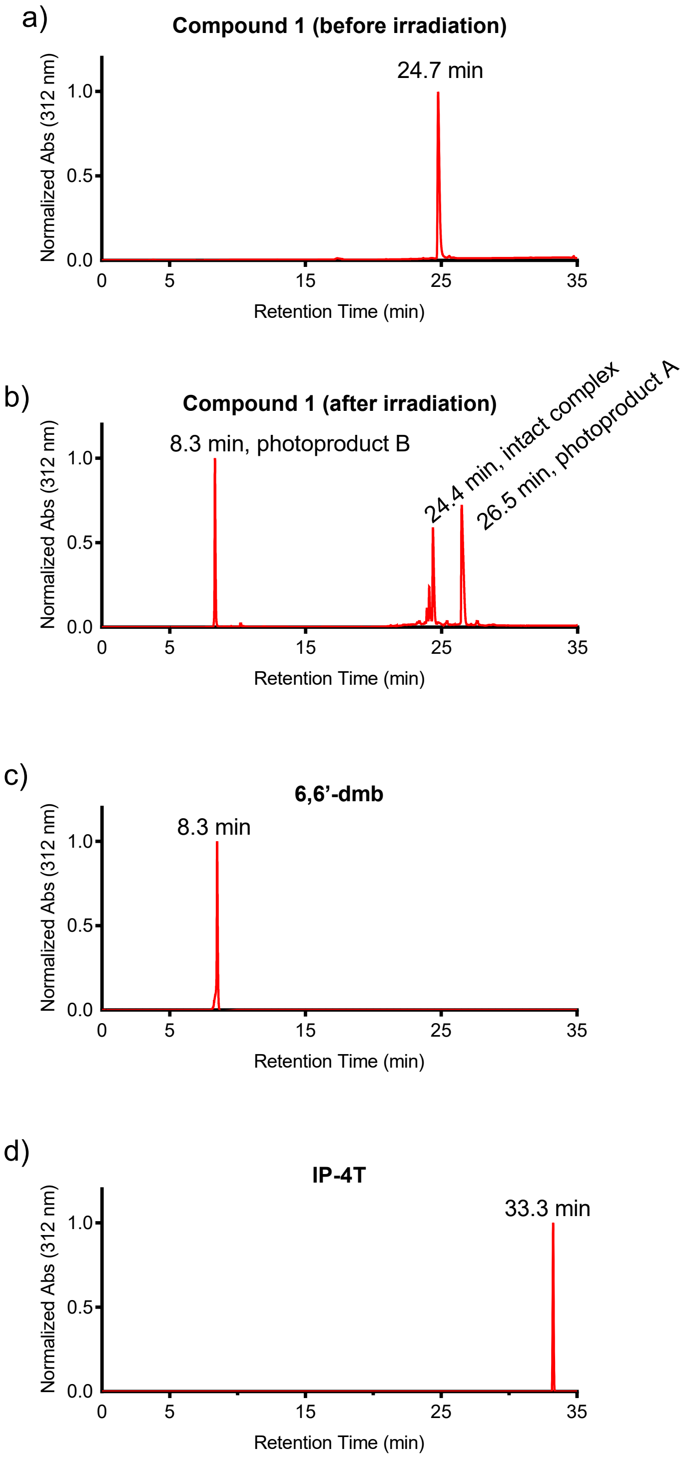

Figure S12. HPLC chromatograms of **1** before irradiation (a) and after irradiation (b) compared to those of the free ligands 6,6′-dmb (c) and IP-4T (d). The retention time of photoproduct B matches that of the free 6,6′-dmb ligand, whereas photoproduct A has a retention time that is slightly longer than intact complex **1**. Free IP-4T was not detected in the irradiated sample. Thus, we assign photoproduct B as the photodissociated 6,6′-dmb ligand and photoproduct A as the solvated Ru(II) complex.

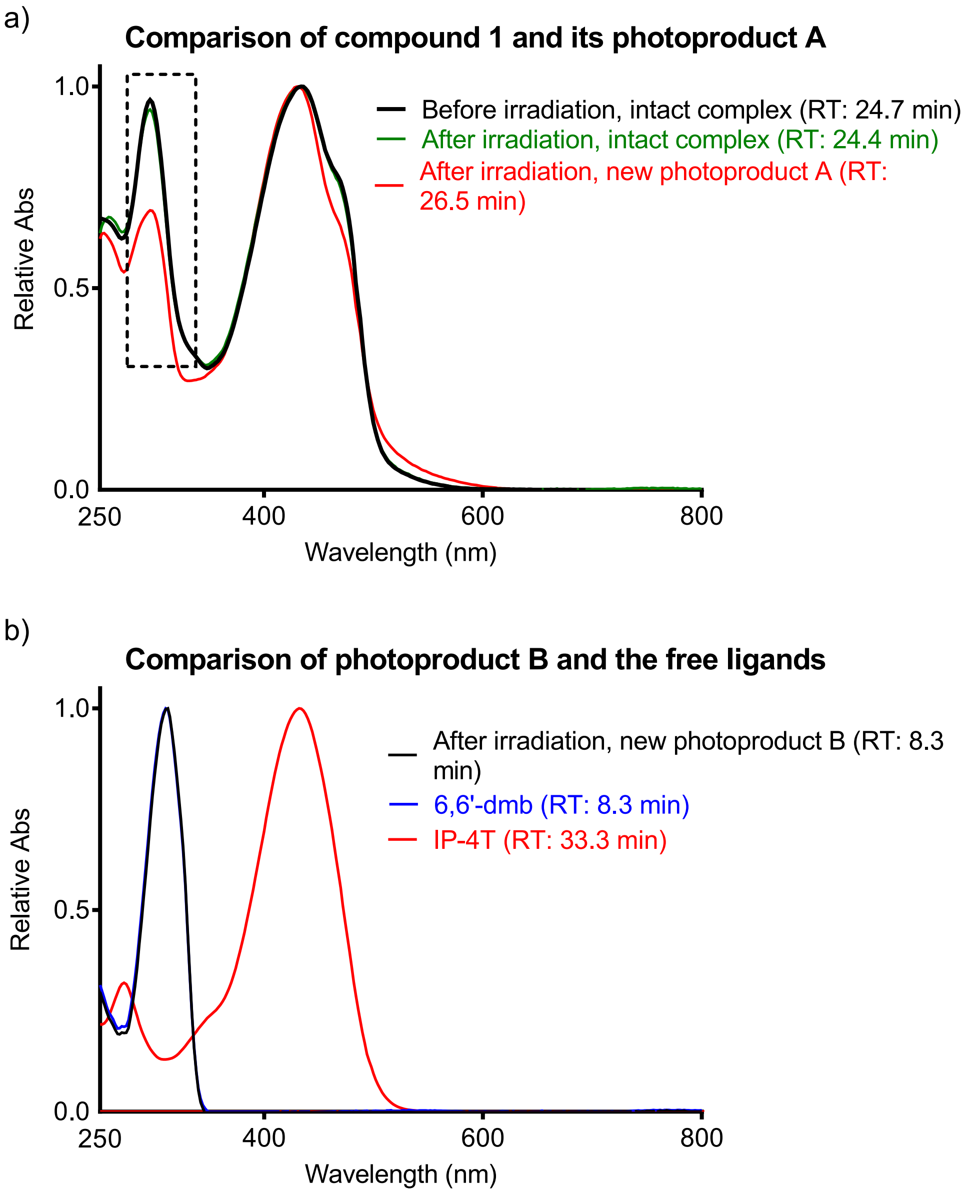

Figure S13. UV-Vis absorption spectra for the HPLC peaks shown in Figure S12. (a) Comparison of the spectrum for the peak at 24.7 min (intact complex) before irradiation with the spectra for the peaks at 24.4 min (intact complex) and 26.5 min (photoproduct A) after irradiation. (b) Comparison of the spectrum for the peak at 8.3 min (photoproduct B) with the spectra for the peaks from the free 6,6′-dmb and IP-4T ligands that occur at 8.3 and 33.3 min, respectively. Thus, we assign photoproduct B as the photodissociated 6,6′-dmb ligand (due to its exact match in terms of retention time and absorption profile with the free 6,6′-dmb ligand) and photoproduct A as the solvated Ru(II) complex (due to its MLCT absorption alongside a prominent decrease in the shorter-wavelength region where the bound 6,6′-dmb ligand absorbs, see dashed box).

Compound **1** before irradiation

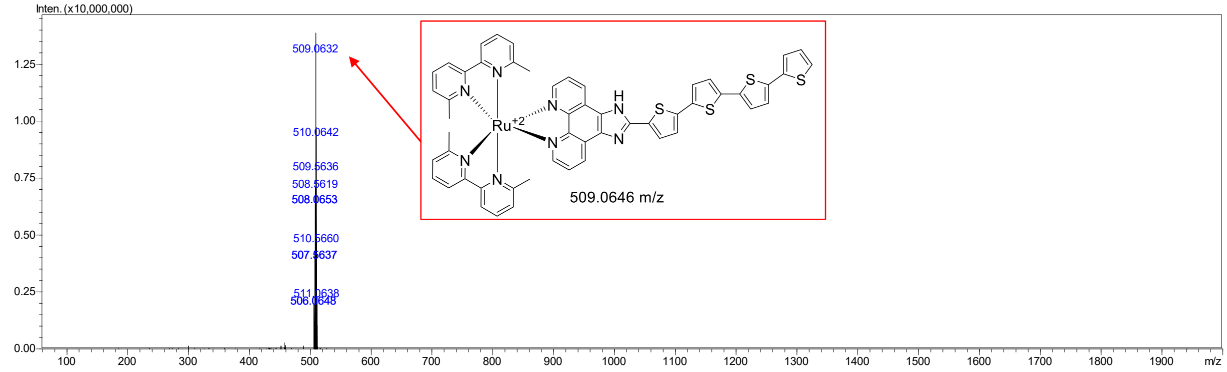

Compound **1** after irradiation

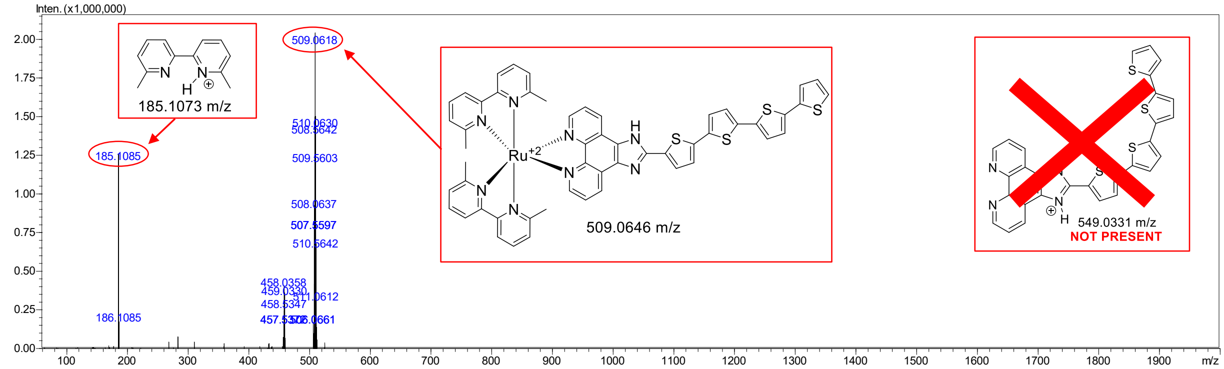

Figure S14. ESI$^+$ MS in MeOH of **1** before and after irradiation. The photodissociated 6,6′-dmb ligand is detected. The absence of a peak for IP-4T suggests that only 6,6′-dmb is lost during the photoreaction.

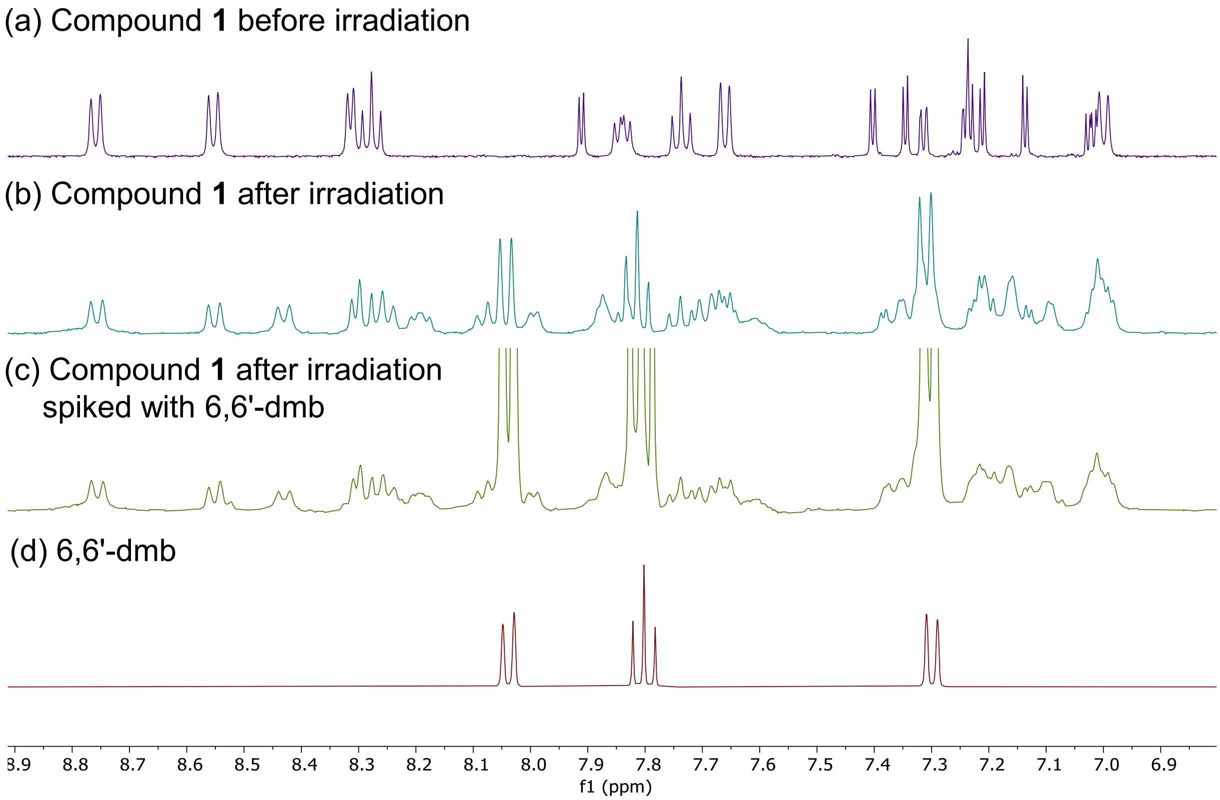

Figure S15. Comparison of the aromatic region of the ^{1}H NMR (500 MHz) spectrum of **1** (Cl$^-$ salt) in MeOD-d_3 at 298 K before (a) and after (b) irradiation. The ^{1}H NMR spectra of the irradiated sample of **1** spiked with 6,6'-dmb (c) and the free 6,6'-dmb ligand in MeOD-d_3 (d) are included to verify that the photoreaction involves the loss of the 6,6'-dmb ligand upon irradiation.

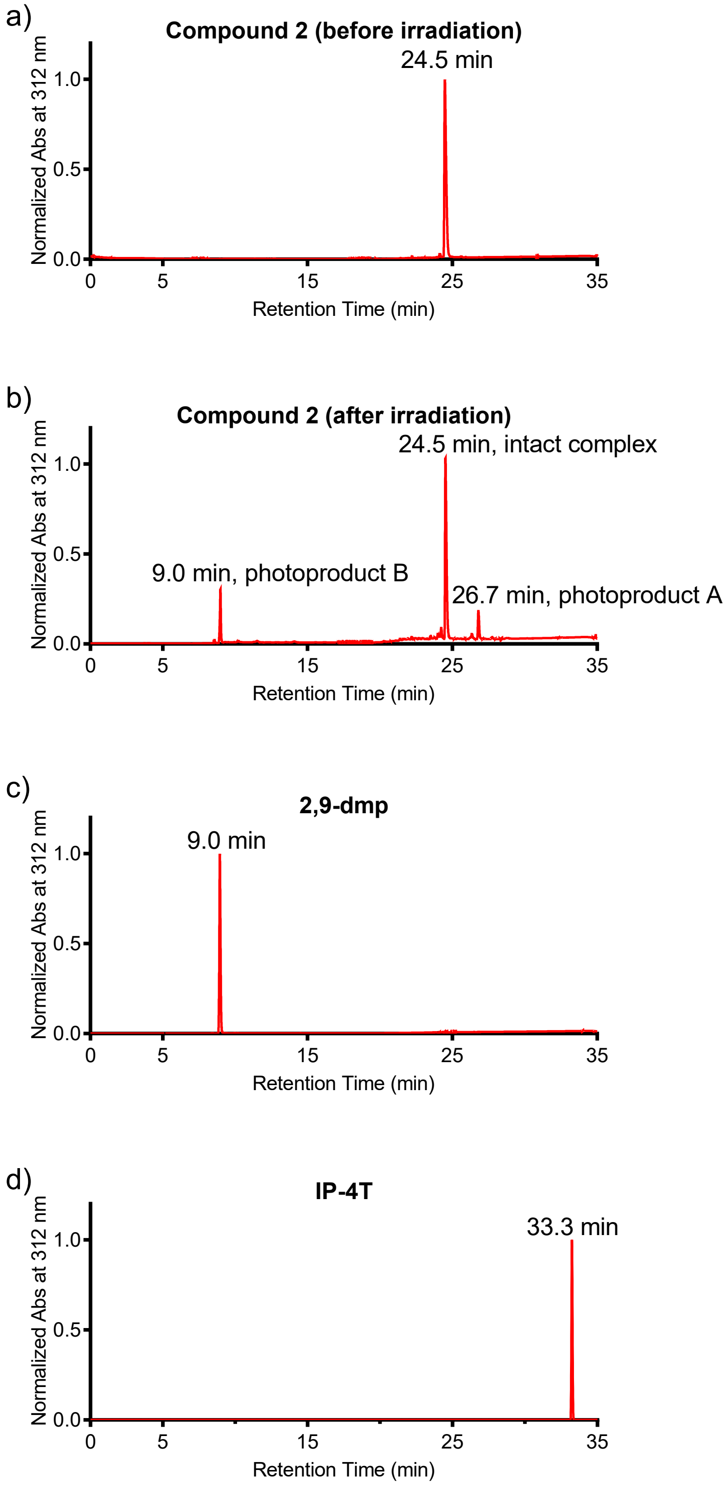

Figure S16. HPLC chromatograms of **2** before irradiation (a) and after irradiation (b) compared to those of the free ligands 2,9-dmp (c) and IP-4T (d). The retention time of photoproduct B matches that of the free 2,9-dmp ligand, whereas photoproduct A has a retention time that is slightly longer than intact complex **2**. Free IP-4T was not detected in the irradiated sample. Thus, we assign photoproduct B as the photodissociated 2,9-dmp ligand and photoproduct A as the resulting aquated Ru(II) complex.

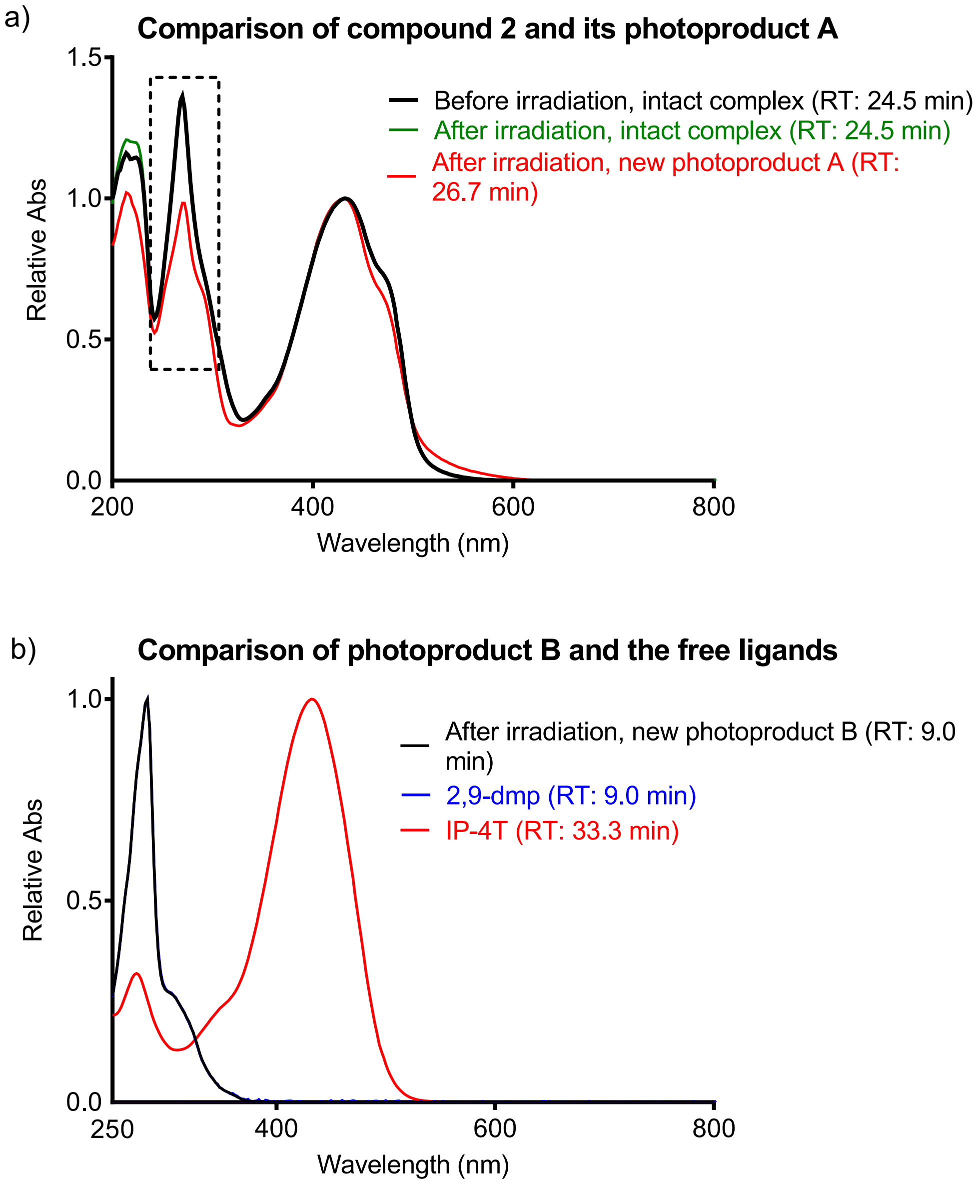

Figure S17. UV-Vis absorption spectra of **2** before and after irradiation. a) Overlay of UV-Vis traces of **2** (before and after irradiation) and the photoejected complex; b) UV-Vis spectra of the photoejected ligand compared with free ligands 2,9-dmp and IP-4T. (b) Comparison of the spectrum for the peak at 9.0 min (photoproduct B) with the spectra for the peaks from the free 2,9-dmp and IP-4T ligands that occur at 9.0 and 33.3 min, respectively. Thus, we assign photoproduct B as the photodissociated 2,9-dmp ligand (due to its exact match in terms of retention time and absorption profile with the free 2,9-dmp ligand) and photoproduct A as the solvated Ru(II) complex (due to its MLCT absorption alongside a prominent decrease in the shorter-wavelength region where the bound 2,9-dmp ligand absorbs, see dashed box).

Compound **2** before irradiation

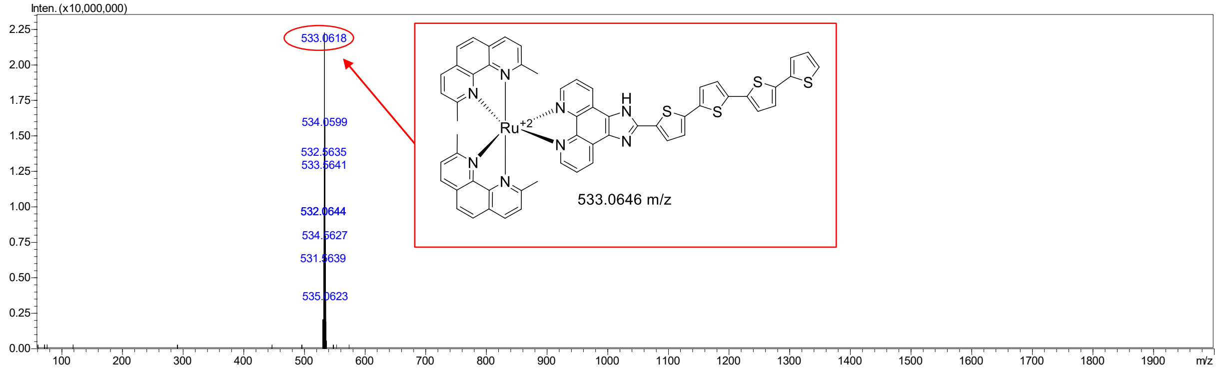

Compound **2** after irradiation

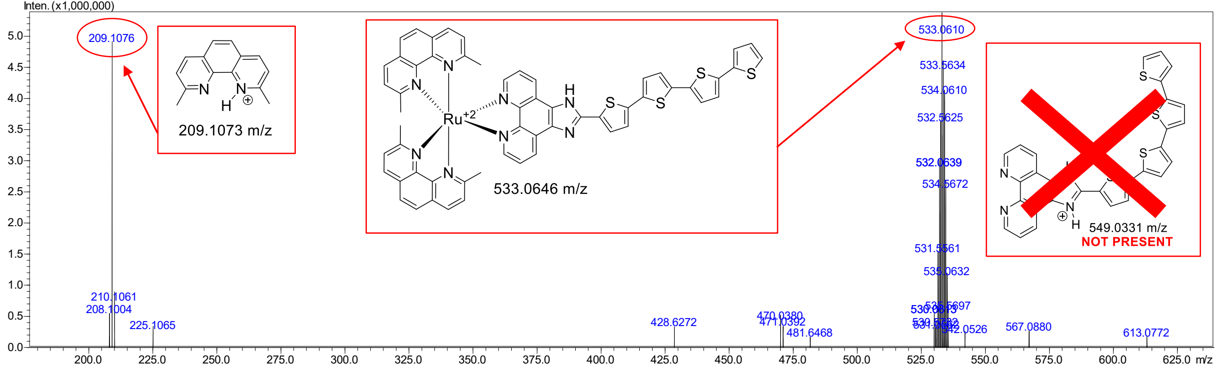

Figure S18. ESI$^+$ MS in MeOH of **2** before and after irradiation. The photodissociated 2,9-dmp ligand is detected. The absence of a peak for IP-4T suggests that only 2,9-dmp is lost during the photoreaction.

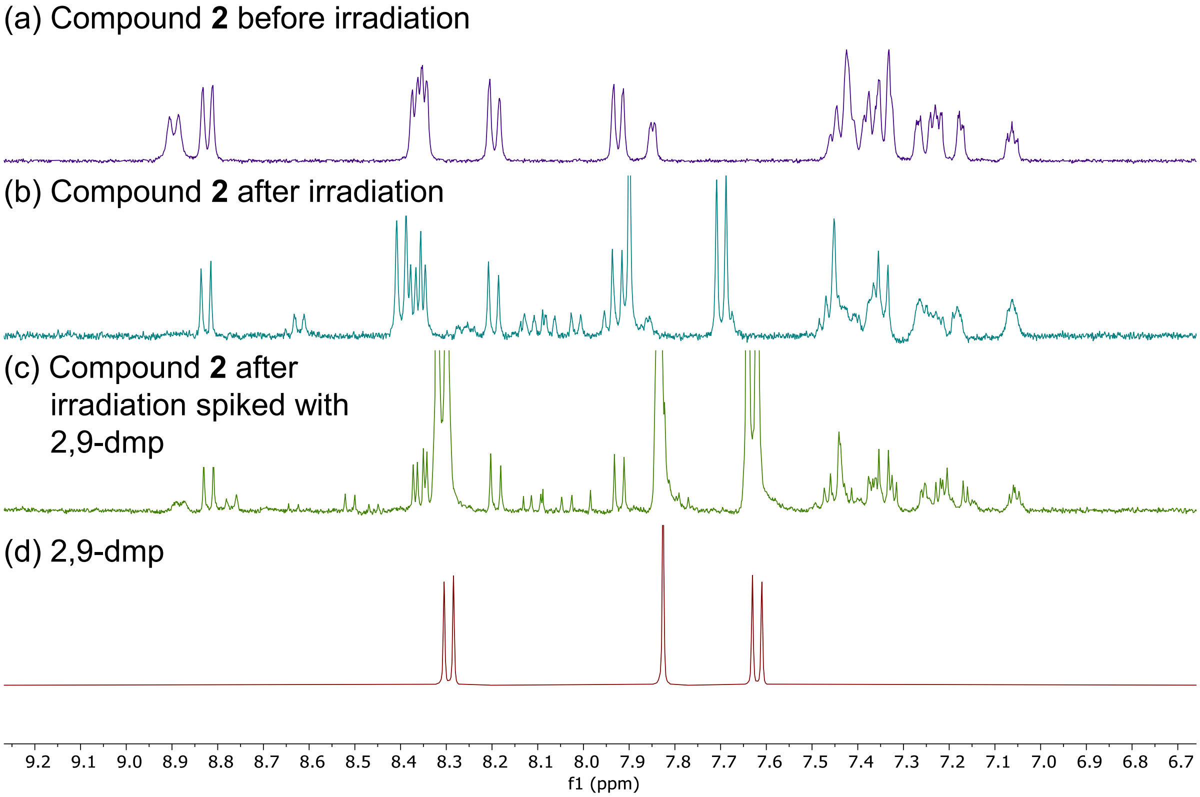

Figure S19. Comparison of the aromatic region of the ^{1}H NMR (500 MHz) spectrum of **2** (Cl^- salt) in MeOD-*d*$_3$ at 298 K before (a) and after (b) irradiation. The ^{1}H NMR spectra of the irradiated sample of **2** spiked with 2,9-dmp (c) and the free 2,9-dmp ligand in MeOD-*d*$_3$ (d) are included to verify that the photoreaction involves the loss of the 2,9-dmp ligand upon irradiation.

7. BIOLOGICAL AND PHOTOBIOLOGICAL DATA

7.1 Subculture

All cell lines were adherent and subcultured at ≥90% relative humidity, 37°C, and either 5 or 10% CO_2, depending whether EMEM (5% CO_2) or DMEM (10% CO_2) was in use. Cells were split at ATCC recommended ratios and given fresh media every 2 or 3 days. Cells were used in cellular assays after at least two passages from thawing, each with no more than 15 passages from receipt at time of screening. Cells were frozen according to ATCC guidelines and each brought up and spun down at 125×g for 10 min prior to subculture.

7.1.1 A549

Male lung carcinoma A549 cells (ATCC CCL-185) were subcultured and screened using EMEM (BioWhittaker, 12-125Q) supplemented with 10% FB essence (VWR, 10803-034) and 1% glutagro (L-alanyl-L-glutamine; VWR 45001-086). To 384-well plates for cytotoxicity screening, the cells were seeded at 225,000 cells mL^{-1} (4500 cells $well^{-1}$).

7.1.2 B16F10

Highly pigmented (melanotic) murine B16-F10 cells (ATCC CRL-6475) were subcultured using high-glucose DMEM (Cytiva SH30243.01) supplemented with 10% FB essence (VWR, 10803-034) and 1% glutagro (L-alanyl-L-glutamine; VWR 45001-086). The media was changed to EMEM several hours in advance of setting up the assay to facilitate hypoxic culture at 5% CO_2. To 384-well plates for cytotoxicity screening, the cells were seeded at 200,000 cells mL^{-1} (4000 cells $well^{-1}$).

7.1.3 MCF7

Female mammary adenocarcinoma MCF7 cells (ATCC HTB-22) were subcultured using high-glucose DMEM (Cytiva SH30243.01) supplemented with 10% FB essence (VWR, 10803-034) and 1% glutagro (L-alanyl-L-glutamine; VWR 45001-086). The media was changed to EMEM several hours in advance of splitting the cells for the assay to facilitate hypoxic culture at 5% CO_2. To 384-well plates for cytotoxicity screening, the cells were seeded at 275,000 cells mL^{-1} (5500 cells $well^{-1}$).

7.1.4 SKMEL28

Male amelanotic melanoma SK-MEL-28 cells (ATCC HTB-72) were subcultured and screened using EMEM (BioWhittaker, 12-125Q) supplemented with 10% FB essence (VWR, 10803-034) and 1% glutagro (L-alanyl-L-glutamine; VWR 45001-086). To 384-well plates for cytotoxicity screening, the cells were seeded at 150,000 cells mL^{-1} (3000 cells $well^{-1}$).

7.2 Measuring Dissolved Oxygen

Dissolved oxygen was measured prior to irradiation of hypoxic well plates using an immersive optical probe inside the Biospherix culture chamber. The values were: A549: 5-9 μM; B16F10: 4.5-9 μM; MCF7: 5.5-9 μM; and SKMEL28: 6.6-9.5 μM. As seen in Figure S20 we applied the Pyroscience FSO2-C1 meter and measured dissolved O_2 (μM) after a 2 point calibration using their ultra-high speed retractable needle sensor (PS OXR430-UHS). These are also available from Pyroscience's US-based distributor, Ohio-Lumex. Various items were purchased from Thorlabs for fabricating a micromanipulator for measurements in the 384 well plates.

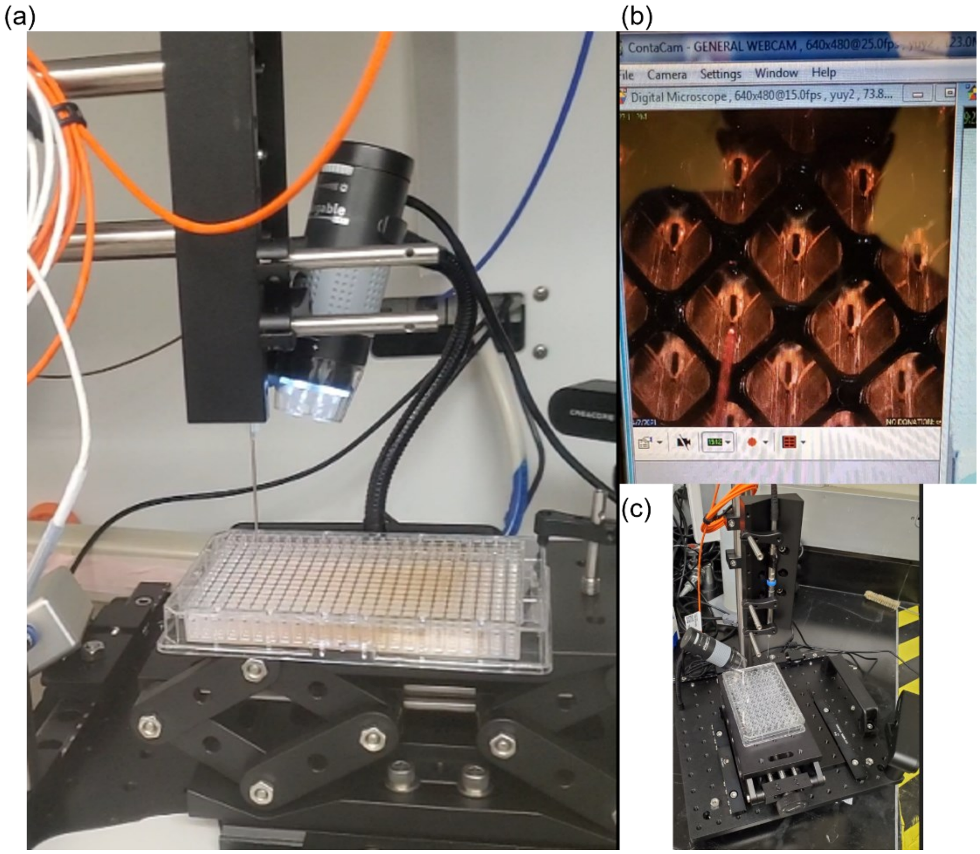

Figure S20. Set-up for measuring dissolved O_2 in the assays. (a) dO_2 probe positioned above well plate measurements inside the Biospherix chamber, (b) digital micrograph of probe sensor, flashing red above a well, and (c) side-view of mock set-up on the bench.

7.3 Cytotoxic and Photocytotoxic Assays

Compounds **1** and **2** were prepared at 5 mM in 10% DMSO:H_2O and 25 mM in DMSO, respectively, in foil-covered vials with PTFE-lined caps. Stock solutions were stored at −20°C when not in use and generally aliquoted into room temperature 1× DPBS by reverse pipette technique. Dilutions were prepared in serial in DPBS using the same tip and rinsing several times prior to subsequent dilutions.

The compounds were screened from 300 μM to 1×10^{-12} μM in clear 384-well plates (Greiner Bio-One 781182) as previously described using the resazurin viability assay.[13–15] Cells were first seeded and allowed to adhere for 2–3h (normoxia, ~18.5% O_2) before placing hypoxic-treated plates in the Biospherix XVivo X3 at 1% O_2, 5% CO_2, and 37°C for an additional 2–3h as a conditioning step for hypoxia. After a total of 4–6h incubation under their respective oxygen culture conditions, both sets of plates were treated with compound and allowed to incubate overnight for an additional 16h (drug-to-light interval, DLI) prior to either light treatment (100 J cm^{-2}, ~20 mW cm^{-2}; sources shown in Figure S23) or reference dark treatment (0 J cm^{-2}). Hypoxic plates were sealed for the period of irradiation using qPCR films (VWR, 89134-428) Plates were again allowed to incubate overnight; however, both normoxic and hypoxic sets were placed in the normoxic incubator to mitigate interference of the resazurin assay as previously described.[1,3,12,16] Following this 20h incubation in normoxia, resazurin dye was dispensed and data corrected for background (cell-free; media+DPBS) and normalized to positive growth controls. Three parameter log-logistic and logistic fits (Equation S6 and Equation S7, four-parameter shown, where bottom is constrained to equal zero and X is equal to concentration) were applied to the datasets with bottom=0 due to background correction. A combination of r script[17] (dplyr,[18] openxlsx,[19] plater[20] packages) and GraphPad Prism 9.1 was used for data processing and plotting.

$$Y = \mathrm{Bottom} + \frac{(Top - Bottom)}{(1 + (10^{Log(EC_{50} - X) \times Hillslope})} \quad \text{Equation S6}$$

$$Y = \mathrm{Bottom} + \frac{(Top - Bottom)}{\left(1 + (EC_{50}/X)^{Hillslope}\right)} \quad \text{Equation S7}$$

Replicates are always plotted ± standard deviation (SD) on a plot. Reported EC_{50} values are ± SEM for a given experiment; these denote the effective concentration to reduce relative cell viability by 50% of the fitted curve (EC_{50}) ± standard error of the mean (SEM). Steep hill slopes with ambiguous confidence intervals are unable to determine the SEM and labelled as not determined (n.d.). Phototherapeutic indices (PI) are reported as the ratio of dark to light EC_{50} values and used as a measure of light-induced potency. Summary activity plots used for quickly comparing compound potency (Log EC_{50}, PI, and Log PI) include SEM from log-logistic fits where applicable (Log EC_{50}).

Table S1. Cytotoxicity and photocytotoxicity of **1** and **2** in hypoxic (1% O_2) or normoxic (18.5–21% O_2) treated A549, B16F10, MCF7 and SKMEL28 cells. Table sorted by oxygen%, cell line, then complex.

Cell line	Complex	Oxygen%	**Resazurin-Cell Viability**								
			EC$_{50}$ ± SEM (μM)					PI[e]			
			Dark	Visible[a]	Blue[b]	Green[c]	Red[d]	Visible[a]	Blue[b]	Green[c]	Red[d]
A549	**1**	1	56.5 ± 4.5	60.8 ± 2.8	52.0 ± 4.0	1.08 ± 2.15	50.8 ± 1.8	1	1	52	1
	2	1	72.7 ± 2.9	0.143 ± n.d.	0.131 ± n.d.	1.22 ± n.d.	80.4 ± 2.4	508	555	60	1
B16F10	**1**	1	55.4 ± 2.3	52.5 ± 1.7	56.6 ± 2.0	49.6 ± 2.3	53.4 ± 1.4	1	1	1	1
	2	1	78.6 ± 2.5	0.144 ± 0.050	0.139 ± 0.084	1.190 ± n.d.	79.2 ± 2.5	546	565	66	1
MCF7	**1**	1	73.6 ± 2.0	63.8 ± 1.5	59.7 ± 2.4	61.4 ± 3.7	71.3 ± 1.2	1	1	1	1
	2	1	87.1 ± 1.8	118 ± 5	104 ± 4	115 ± 5	87.3 ± 2.3	1	1	1	1
SKMEL28	**1**	1	70.9 ± 1.2	1.16 ± n.d.	1.10 ± n.d.	0.443 ± 0.030	69.6 ± 1.6	61	64	160	1
	2	1	78.4 ± 1.6	0.0133 ± 0.0030	(7.35 ± 2.06)$\times10^{-3}$	0.0156 ± 0.0009	80.2 ± 1.6	5895	10667	5026	1
A549	**1**	~18.5	50.0 ± 1.9	0.0156 ± n.d.	0.0151 ± 0.0088	0.0250 ± 0.0060	16.9 ± 1.7	3205	3311	2000	3
	2	~18.5	79.4 ± 2.0	(6.17 ± n.d.)$\times10^{-4}$	(6.15 ± n.d.)$\times10^{-4}$	0.0149 ± n.d.	17.4 ± 3.7	128687	129106	5329	5
B16F10	**1**	~18.5	54.0 ± 1.7	0.0197 ± 0.0024	0.0139 ± 0.0018	0.0331 ± 0.0052	16.9 ± 2.4	2741	3885	1631	3
	2	~18.5	78.3 ± 2.1	(2.81 ± 0.33)$\times10^{-4}$	(3.16 ± 0.49)$\times10^{-4}$	(6.05 ± 3.34)$\times10^{-3}$	16.7 ± 3.9	278648	247785	12942	5
MCF7	**1**	~18.5	73.1 ± 1.7	0.0301 ± 0.0053	0.0306 ± 0.0026	0.137 ± 0.010	27.6 ± 1.1	2429	2389	534	3
	2	~18.5	93.9 ± 2.2	(7.86 ± n.d.)$\times10^{-4}$	(6.99 ± n.d.)$\times10^{-4}$	0.0214 ± 0.0025	51.5 ± 0.6	119466	134335	4388	2
SKMEL28	**1**	~18.5	76.2 ± 1.6	0.0198 ± 0.0037	0.0223 ± 0.0054	0.0328 ± 0.0033	16.5 ± 1.9	3848	3417	2323	5
	2	~18.5	89.6 ± 2.1	(1.70 ± n.d.)$\times10^{-4}$	(2.60 ± 0.21)$\times10^{-4}$	(1.33 ± 0.09)$\times10^{-3}$	14.3 ± 0.6	527059	344615	67368	6

Light treatments were approximately 100 J cm^{-2} delivered at 18–24 mW cm^{-2} with [a] cool white Visible (400–700 nm), [b] Blue (453 nm), [c] Green (523 nm), [d] Red (633 nm), and [e] PI = phototherapeutic index. Hypoxia and normoxia experiments were ran in parallel. Two experiments with either (i) A549 and B16F10 or (ii) MCF7 and SKMEL28 cells were run within a week of each other. *n.d. = SEM not determined due to steep hill slope.

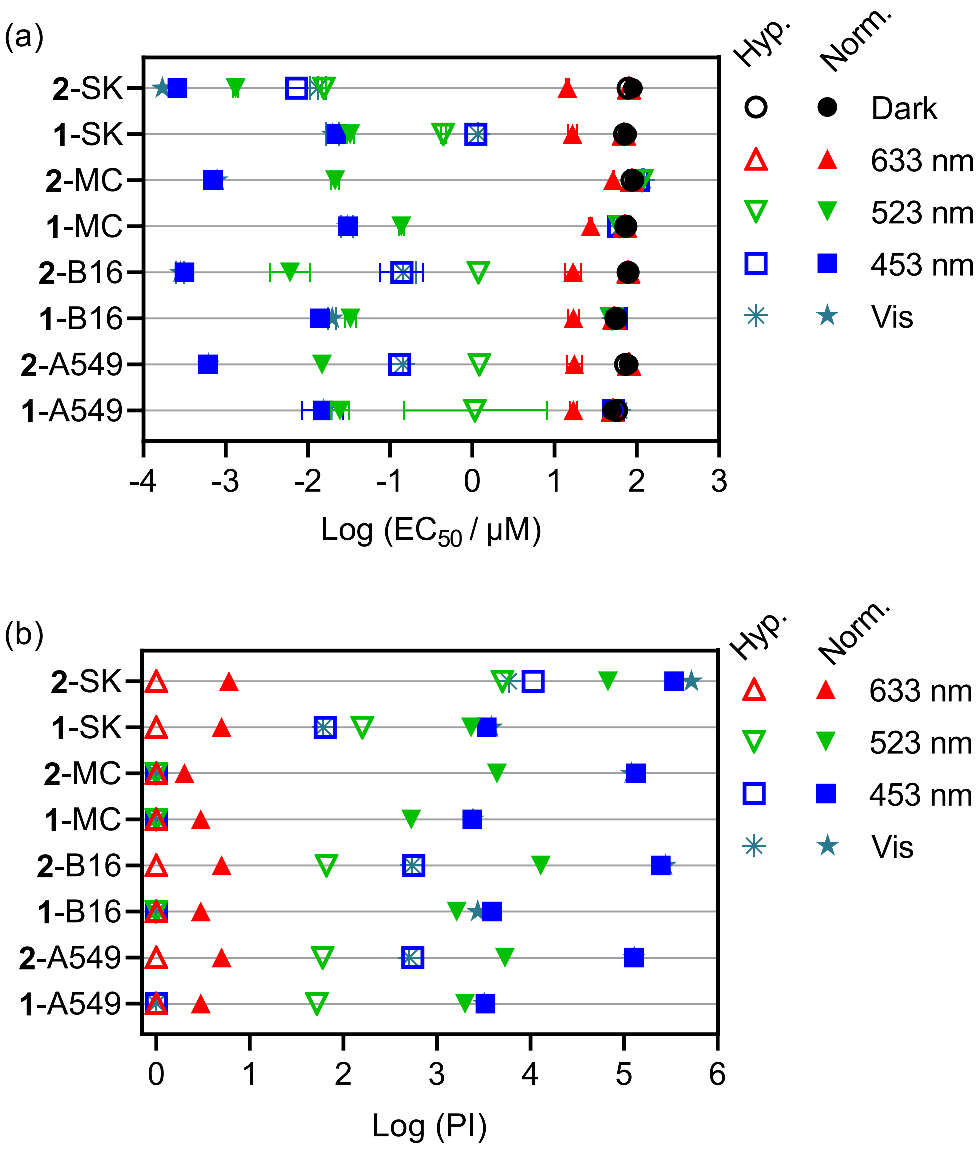

Figure S21. Summary cytotoxicity (dark) and photocytotoxicity (a) best-fit log (EC_{50}±SEM) values and (b) phototherapeutic indices (PI; dark EC_{50}/light EC_{50}). Cell lines are listed in order of A549, B16F10, MCF7, and SKMEL28. Unfilled symbols correspond to hypoxic treatment (1% O_2) and filled to normoxic treatment (18.5–21% O_2).

Table S2. Alternative format of Table S1. Cytotoxicity and photocytotoxicity of **1** and **2** in hypoxic (1% O_2) or normoxic (18.5–21% O_2) treated A549, B16F10, MCF7 and SKMEL28 cells. Table sorted by oxygen%, complex, then cell line.

Complex	Cell line	Oxygen%	**Resazurin-Cell Viability**								
			EC_{50} ± SEM (μM)					PI[e]			
			Dark	Visible[a]	Blue[b]	Green[c]	Red[d]	Visible[a]	Blue[b]	Green[c]	Red[d]
1	A549	1	56.5 ± 4.5	60.8 ± 2.8	52.0 ± 4.0	1.08 ± 2.15	50.8 ± 1.8	1	1	52	1
1	B16F10	1	55.4 ± 2.3	52.5 ± 1.7	56.6 ± 2.0	49.6 ± 2.3	53.4 ± 1.4	1	1	1	1
1	MCF7	1	73.6 ± 2.0	63.8 ± 1.5	59.7 ± 2.4	61.4 ± 3.7	71.3 ± 1.2	1	1	1	1
1	SKMEL28	1	70.9 ± 1.2	1.16 ± n.d.	1.10 ± n.d.	0.443 ± 0.030	69.6 ± 1.6	61	64	160	1
2	A549	1	72.7 ± 2.9	0.143 ± n.d.	0.131 ± n.d.	1.22 ± n.d.	80.4 ± 2.4	508	555	60	1
2	B16F10	1	78.6 ± 2.5	0.144 ± 0.050	0.139 ± 0.084	1.190 ± n.d.	79.2 ± 2.5	546	565	66	1
2	MCF7	1	87.1 ± 1.8	118 ± 5	104 ± 4	115 ± 5	87.3 ± 2.3	1	1	1	1
2	SKMEL28	1	78.4 ± 1.6	0.0133 ± 0.0030	$(7.35 \pm 2.06)\times10^{-3}$	0.0156 ± 0.0009	80.2 ± 1.6	5895	10667	5026	1
1	A549	~18.5	50.0 ± 1.9	0.0156 ± n.d.	0.0151 ± 0.0088	0.0250 ± 0.0060	16.9 ± 1.7	3205	3311	2000	3
1	B16F10	~18.5	54.0 ± 1.7	0.0197 ± 0.0024	0.0139 ± 0.0018	0.0331 ± 0.0052	16.9 ± 2.4	2741	3885	1631	3
1	MCF7	~18.5	73.1 ± 1.7	0.0301 ± 0.0053	0.0306 ± 0.0026	0.137 ± 0.010	27.6 ± 1.1	2429	2389	534	3
1	SKMEL28	~18.5	76.2 ± 1.6	0.0198 ± 0.0037	0.0223 ± 0.0054	0.0328 ± 0.0033	16.5 ± 1.9	3848	3417	2323	5
2	A549	~18.5	79.4 ± 2.0	$(6.17 \pm \text{n.d.})\times10^{-4}$	$(6.15 \pm \text{n.d.})\times10^{-4}$	0.0149 ± n.d.	17.4 ± 3.7	128687	129106	5329	5
2	B16F10	~18.5	78.3 ± 2.1	$(2.81 \pm 0.33)\times10^{-4}$	$(3.16 \pm 0.49)\times10^{-4}$	$(6.05 \pm 3.34)\times10^{-3}$	16.7 ± 3.9	278648	247785	12942	5
2	MCF7	~18.5	93.9 ± 2.2	$(7.86 \pm \text{n.d.})\times10^{-4}$	$(6.99 \pm \text{n.d.})\times10^{-4}$	0.0214 ± 0.0025	51.5 ± 0.6	119466	134335	4388	2
2	SKMEL28	~18.5	89.6 ± 2.1	$(1.70 \pm \text{n.d.})\times10^{-4}$	$(2.60 \pm 0.21)\times10^{-4}$	$(1.33 \pm 0.09)\times10^{-3}$	14.3 ± 0.6	527059	344615	67368	6

Light treatments were approximately 100 J cm^{-2} delivered at 18–24 mW cm^{-2} with [a] cool white Visible (400–700 nm), [b] Blue (453 nm), [c] Green (523 nm), [d] Red (633 nm), and [e] PI = phototherapeutic index. Hypoxia and normoxia experiments were ran in parallel. Two experiments with either (i) A549 and B16F10 or (ii) MCF7 and SKMEL28 cells were ran within a week of each other. *n.d. = SEM not determined due to steep hill slope.

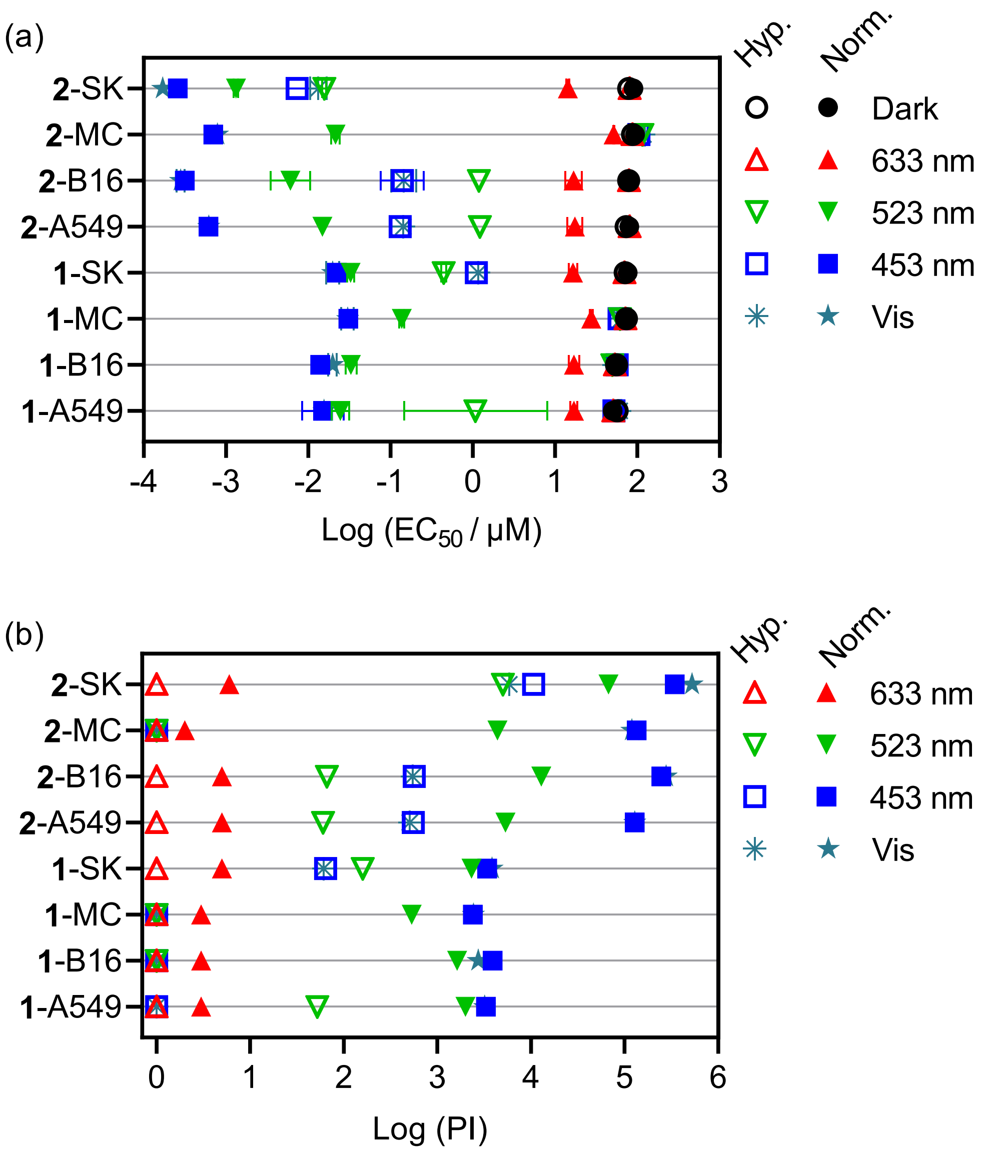

Figure S22. Alternative order on y-axis. Summary cytotoxicity (dark) and photocytotoxicity (a) best-fit log (EC_{50}±SEM) values and (b) phototherapeutic indices (PI; dark EC_{50}/light EC_{50}). Cell lines are listed in order of A549, B16F10, MCF7, and SKMEL28. Unfilled symbols correspond to hypoxic treatment (1% O_2) and filled to normoxic treatment (18.5–21% O_2).

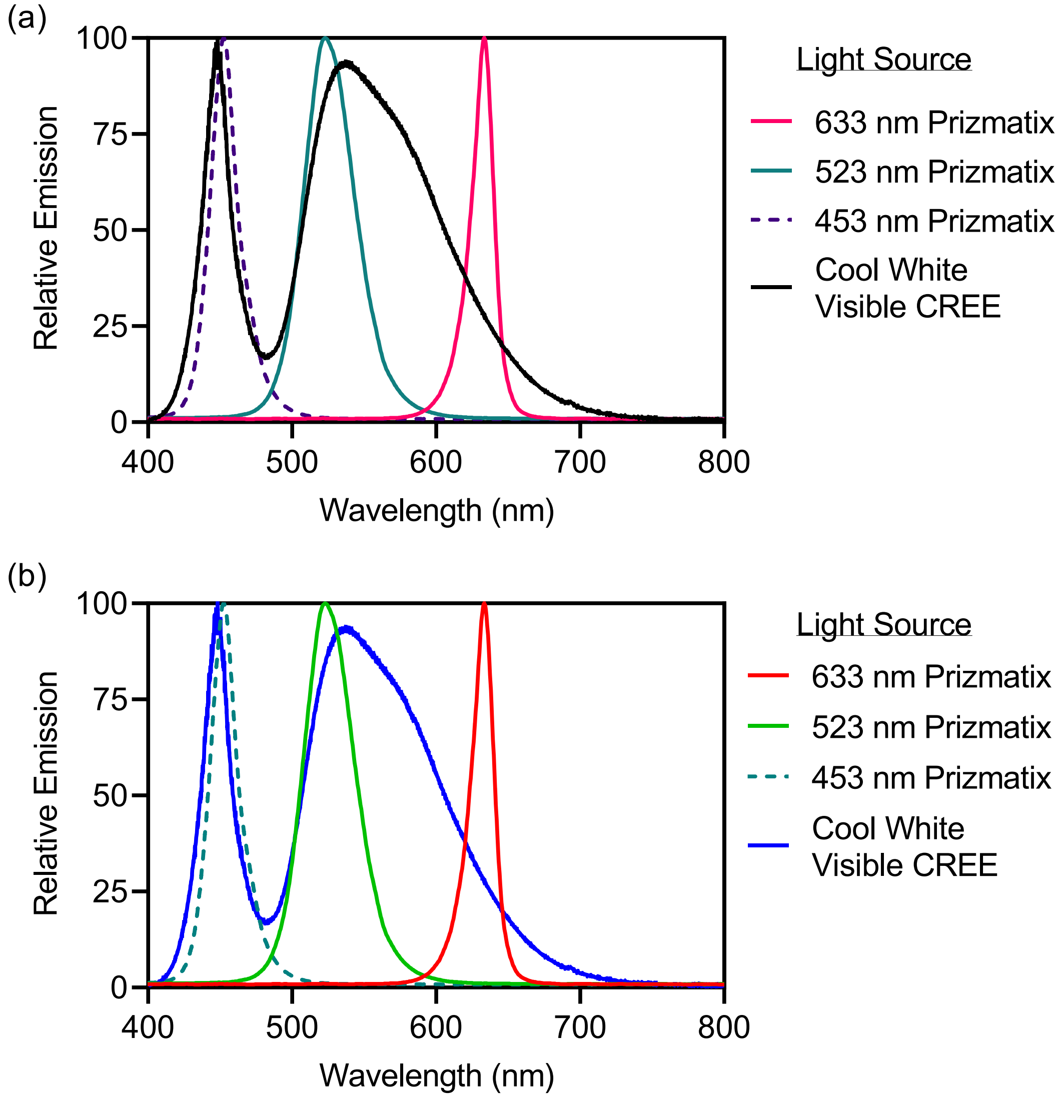

Figure S23. Light sources applied in photobiological and photochemical studies where (a) uses a colorblind friendly scheme and (b) approximately matches the spectral output color.

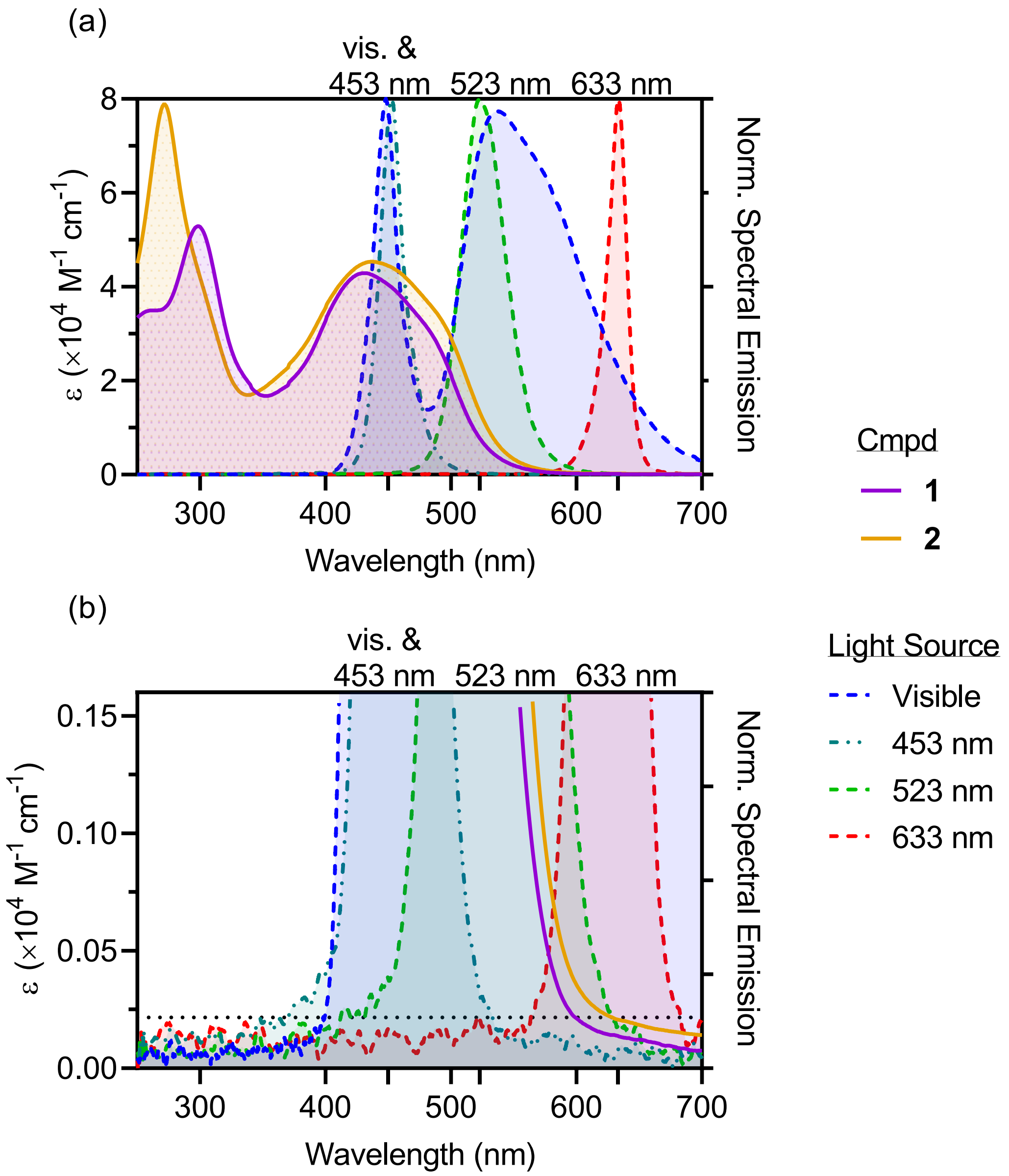

Figure S24. Spectral overlay of **1** and **2** in water (left y-axis) and normalized light source outputs or emissions (right y-axis) with full scale in (a) and a zoom in (b). The dotted line in (b) indicates the threshold used for any absorbed photon estimates, as applied in photosubstitution quantum yields. Area fill was excluded in the spectra of **1** and **2** in (b).

Note that Figure S24 uses the spectrum of **2** after equilibration in the absence of light for ~3h due to propensity to agglomerate.

Table S3. Approximate photon flux density (mol m^{-2} s^{-1}) absorbed by 20 μM **1** and **2** in water (5 mm pathlength; 200 W m^{-2}). A threshold of 0.27% relative light source emission was applied to negate any integral contribution by noise. Does not correct for scatter or reflection. [a]cool white visible (400–700 nm), [b]blue 453 nm, [c]green 523 nm, [d]red 633 nm, [e]ratio of blue to visible absorbed photon flux, [f]ratio of visible to green absorbed photon flux, and [g]ratio of visible to red absorbed photon flux. PS and light source overlay in Figure S24.

Cmpd	Vis[a]	453 nm[b]	523 nm[c]	633nm[d]	B:V[e]	V:G[f]	V:R[g]
1	1.49×10^{-4}	4.14×10^{-4}	1.45×10^{-4}	3.54×10^{-6}	3	1	42
2	1.80×10^{-4}	4.44×10^{-4}	2.13×10^{-4}	5.50×10^{-6}	2	1	33

Table S4. Cytotoxicity and photocytotoxicity evaluation of ligands 6,6'-dmb and 2,9-dmp toward MCF7 and SKMEL28 cells in hypoxia (1% O_2) or normoxia (18.5–21% O_2). Table sorted by oxygen%, cell line, then complex.

Cell line	Complex	Oxygen%	Resazurin-Cell Viability								
			EC$_{50}$ (μM)					PI[e]			
			Dark	Visible[a]	Blue[b]	Green[c]	Red[d]	Visible[a]	Blue[b]	Green[c]	Red[d]
MCF7	**6,6'-dmb**	1	>>300	>>300	>>300	>>300	>>300	–	–	–	–
	2,9-dmp	1	>>300	>>300	>>300	>>300	>>300	–	–	–	–
SKMEL28	**6,6'-dmb**	1	>>300	>>300	>>300	>>300	>>300	–	–	–	–
	2,9-dmp	1	>>300	>>300	>>300	>>300	>>300	–	–	–	–
MCF7	**6,6'-dmb**	~18.5	>>300	>>300	>>300	>>300	>>300	–	–	–	–
	2,9-dmp	~18.5	>>300	>>300	>>300	>>300	>>300	–	–	–	–
SKMEL28	**6,6'-dmb**	~18.5	>>300	>>300	>>300	>>300	>>300	–	–	–	–
	2,9-dmp	~18.5	>>300	>>300	>>300	>>300	>>300	–	–	–	–

Light treatments were approximately 100 J cm^{-2} delivered at 18–24 mW cm^{-2} with [a] cool white Visible (400–700 nm), [b] Blue (453 nm), [c] Green (523 nm), [d] Red (633 nm), and [e] PI = phototherapeutic index. Hypoxia and normoxia experiments were ran in parallel. The EC$_{50}$ values and PIs are undefined over the concentration range tested (1–300 μM).

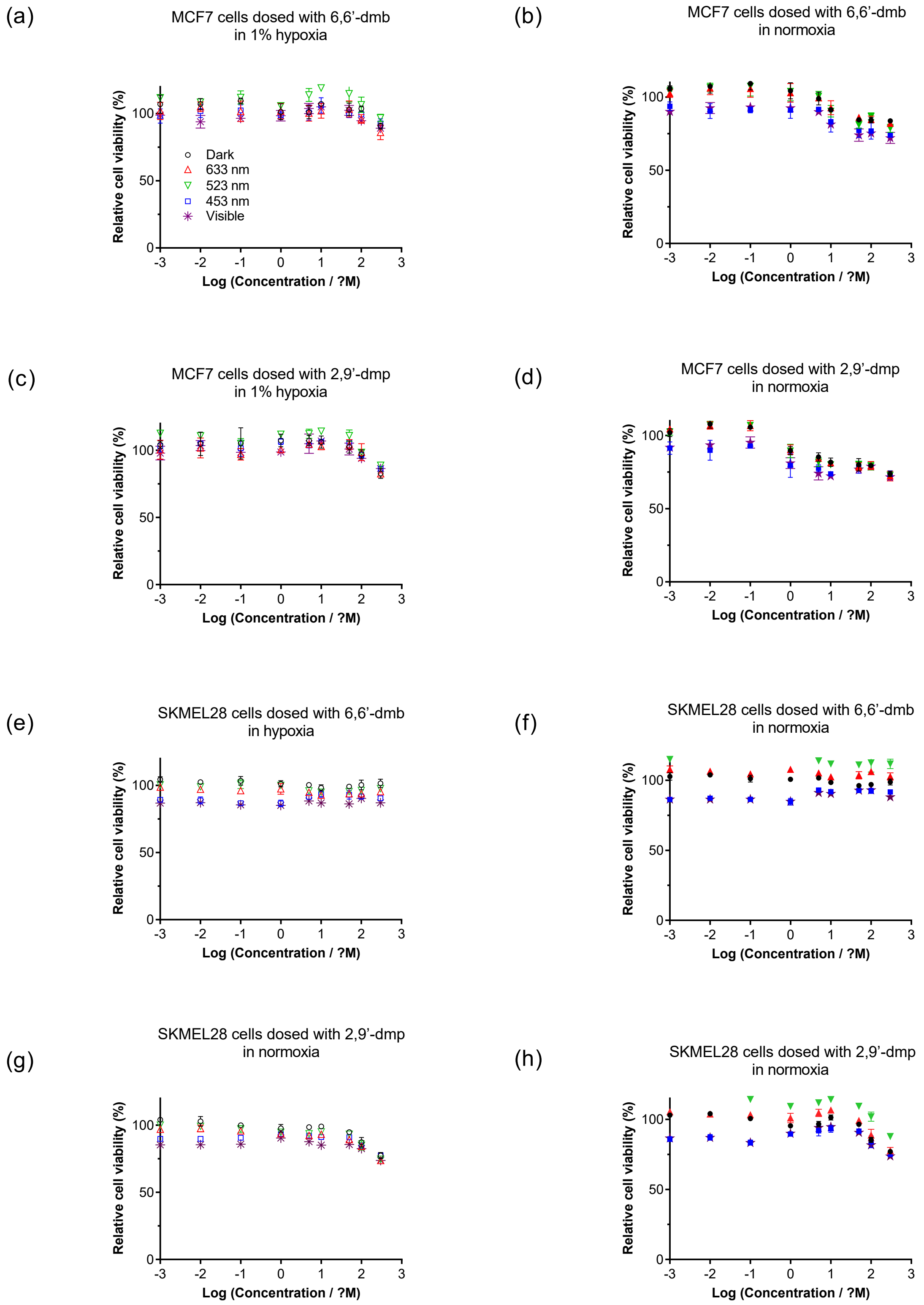

Figure S25. Cytotoxicity and photocytotoxicity dose-response curves (a)-(h) for the free ligands 6,6'-dmb and 2,9-dmp toward MCF7 and SKMEL28 cells in hypoxia (1% O_2) or normoxia (18.5–21% O_2).

8. REFERENCES

(1) Roque III, J. A.; Barrett, P. C.; Cole, H. D.; Lifshits, L. M.; Shi, G.; Monro, S.; von Dohlen, D.; Kim, S.; Russo, N.; Deep, G.; Cameron, C. G.; Alberto, M. E.; McFarland, S. A. Breaking the Barrier: An Osmium Photosensitizer with Unprecedented Hypoxic Phototoxicity for Real World Photodynamic Therapy. *Chem. Sci.* **2020**, *11*, 9784–9806. https://doi.org/10.1039/D0SC03008B.

(2) Pazderski, L.; Pawlak, T.; Sitkowski, J.; Kozerski, L.; Szłyk, E. ^{1}H NMR Assignment Corrections and ^{1}H, ^{13}C, ^{15}N NMR Coordination Shifts Structural Correlations in Fe(II), Ru(II) and Os(II) Cationic Complexes with 2,2′-Bipyridine and 1,10-Phenanthroline. *Magnetic Resonance in Chemistry* **2010**, *48* (6), 450–457. https://doi.org/10.1002/mrc.2600.

(3) Roque, J. A.; Barrett, P. C.; Cole, H. D.; Lifshits, L. M.; Bradner, E.; Shi, G.; von Dohlen, D.; Kim, S.; Russo, N.; Deep, G.; Cameron, C. G.; Alberto, M. E.; McFarland, S. A. Os(II) Oligothienyl Complexes as a Hypoxia-Active Photosensitizer Class for Photodynamic Therapy. *Inorg. Chem.* **2020**, *59* (22), 16341–16360. https://doi.org/10.1021/acs.inorgchem.0c02137.

(4) Tan, L.-F.; Wang, F.; Chao, H.; Zhou, Y.-F.; Weng, C. Ruthenium(II) Mixed-Ligand Complex Containing 2-(4′-Benzyloxy-Phenyl)Imidazo[4,5-f][1,10]Phenanthroline: Synthesis, DNA-Binding and Photocleavage Studies. *Journal of Inorganic Biochemistry* **2007**, *101* (4), 700–708. https://doi.org/10.1016/j.jinorgbio.2006.12.016.

(5) Xu, H.; Zheng, K.-C.; Lin, L.-J.; Li, H.; Gao, Y.; Ji, L.-N. Effects of the Substitution Positions of Br Group in Intercalative Ligand on the DNA-Binding Behaviors of Ru(II) Polypyridyl Complexes. *Journal of Inorganic Biochemistry* **2004**, *98* (1), 87–97. https://doi.org/10.1016/j.jinorgbio.2003.09.002.

(6) Jiang, C.-W.; Chao, H.; Li, R.-H.; Li, H.; Ji, L.-N. Syntheses, Characterization and Third-Order Nonlinear Optical Properties of Ruthenium(II) Complexes Containing 2-Phenylimidazo-[4,5-f][1,10]Phenanthroline and Extended Diimine Ligands. *Polyhedron* **2001**, *20* (17), 2187–2193. https://doi.org/10.1016/S0277-5387(01)00813-0.

(7) DeRosa, M. C.; Crutchley, R. J. Photosensitized Singlet Oxygen and Its Applications. *Coord. Chem. Rev.* **2002**, *233–234*, 351–371. https://doi.org/10.1016/S0010-8545(02)00034-6.

(8) Ogilby, P. R.; Foote, C. S. Chemistry of Singlet Oxygen. 42. Effect of Solvent, Solvent Isotopic Substitution, and Temperature on the Lifetime of Singlet Molecular Oxygen. *Journal of the American Chemical Society* **1983**, *105* (11), 3423–3430. https://doi.org/10.1021/ja00349a007.

(9) Ogilby, P. R. Singlet Oxygen: There Is Still Something New under the Sun, and It Is Better than Ever. *Photochemical & Photobiological Sciences* **2010**, *9* (12), 1543. https://doi.org/10.1039/c0pp00213e.

(10) Bregnhøj, M.; Westberg, M.; Jensen, F.; Ogilby, P. R. Solvent-Dependent Singlet Oxygen Lifetimes: Temperature Effects Implicate Tunneling and Charge-Transfer Interactions. *Phys. Chem. Chem. Phys.* **2016**, *18* (33), 22946–22961. https://doi.org/10.1039/C6CP01635A.

(11) Juris, A.; Balzani, V.; Barigelletti, F.; Campagna, S.; Belser, P.; von Zelewsky, A. Ru(II) Polypyridine Complexes: Photophysics, Photochemistry, Eletrochemistry, and Chemiluminescence. *Coordination Chemistry Reviews* **1988**, *84*, 85–277. https://doi.org/10.1016/0010-8545(88)80032-8.

(12) Roque, J.; Havrylyuk, D.; Barrett, P. C.; Sainuddin, T.; McCain, J.; Colón, K.; Sparks, W. T.; Bradner, E.; Monro, S.; Heidary, D.; Cameron, C. G.; Glazer, E. C.; McFarland, S. A. Strained, Photoejecting Ru(II) Complexes That Are Cytotoxic Under Hypoxic Conditions. *Photochem Photobiol* **2020**, *96* (2), 327–339. https://doi.org/10.1111/php.13174.

(13) Lifshits, L. M.; Roque III, J. A.; Konda, P.; Monro, S.; Cole, H. D.; von Dohlen, D.; Kim, S.; Deep, G.; Thummel, R. P.; Cameron, C. G.; Gujar, S.; McFarland, S. A. Near-Infrared Absorbing Ru(II) Complexes Act as Immunoprotective Photodynamic Therapy (PDT) Agents against Aggressive Melanoma. *Chem. Sci.* **2020**, *11* (43), 11740–11762. https://doi.org/10.1039/D0SC03875J.
(14) Lifshits, L. M.; Roque, J. A.; Cole, H. D.; Thummel, R. P.; Cameron, C. G.; McFarland, S. A. NIR-Absorbing Ru II Complexes Containing A-Oligothiophenes for Applications in Photodynamic Therapy. *ChemBioChem* **2020**, *21*, 3594–3607. https://doi.org/10.1002/cbic.202000419.
(15) Monro, S.; Colón, K. L.; Yin, H.; Roque, J.; Konda, P.; Gujar, S.; Thummel, R. P.; Lilge, L.; Cameron, C. G.; McFarland, S. A. Transition Metal Complexes and Photodynamic Therapy from a Tumor-Centered Approach: Challenges, Opportunities, and Highlights from the Development of TLD1433. *Chem. Rev.* **2019**, *119* (2), 797–828. https://doi.org/10.1021/acs.chemrev.8b00211.
(16) Cole, H. D.; Roque, J. A.; Lifshits, L. M.; Hodges, R.; Barrett, P. C.; Havrylyuk, D.; Heidary, D.; Ramasamy, E.; Cameron, C. G.; Glazer, E. C.; McFarland, S. A. Fine-feature Modifications to Strained Ruthenium Complexes Radically Alter Their Hypoxic Anticancer Activity †. *Photochem Photobiol* **2021**, php.13395. https://doi.org/10.1111/php.13395.
(17) R Core Team. *R: A Language and Environment for Statistical Computing*; R Foundation for Statistical Computing: Vienna, Austria, 2020.
(18) Wickham, H.; François, R.; Henry, L.; Müller, K. *Dplyr: A Grammar of Data Manipulation*; 2020.
(19) Schauberger, P.; Walker, A. *Openxlsx: Read, Write and Edit Xlsx Files*; 2019.
(20) Hughes, S. M. Plater: Read, Tidy, and Display Data from Microtiter Plates. *The Journal of Open Source Software* **2016**, *1* (7), 106. https://doi.org/10.21105/joss.00106.